Captions for Figures in *Evolutionary Quantitative Genetics*, 2023, Oxford University Press

Figure 1.1 Radiograph of a natricine snake showing vertebrae in the body and tail. The distinction between the two kinds of vertebrae is not arbitrary. Ribs are attached to body vertebrae, but not to tail vertebrae. These two vertebral numbers can be assessed, without recourse to radiography, by counting ventral and subcaudal scales. The electronic object is a radiotransmitter used to study thermoregulation in free-ranging females during pregnancy.

Figure 1.2 A five-vertebrae segment of the vertebral column of a natricine snake (*Natrix natrix*), showing functional connections between vertebrae, ribs, and ventral scales. Ribs articulate with the vertebral column, but muscles also connect the tips of the ribs of the ventral scales on the snake's ventral surface. Furthermore, a complicated system of muscles (not shown) connects between the ribs.

Figure 1.3 Distributions of body and tail vertebral numbers in 143 newborn garter snakes, *Thamnophis radix*. (a) Distribution of body vertebral counts. (b) Distribution of tail vertebral counts. Data from Arnold and Bennett (1988).

Figure 1.4 *Drosophila*, showing sites of important bristle counts. (a) Inset showing locations of bristle patches. (b) Sternopleuron location (colored) on the thorax, showing eight sternopleural bristles (c) Abdominal tergites, showing abdominal bristles on the 4th and 5th tergites (colored). After Wheeler (1981).

Figure 1.5 Histograms illustrating variation in *Drosophila melanogaster* bristle counts. (a) Abdominal bristle number (after Falconer 1989). (b) Sternopleuroal bristle number (i.e., sum of right and left sides). This histogram shows just the contributions to total variation from chromosome 2. After Mackay and Lyman (2005).

Figure 1.6 Superficial jaw musculature of three species of Galápagos finches. (a) *Geospiza magnirostris*. (b) *Geospiza fortis*. (c) *Geospiza fuliginosa*.
From Grant (1986) with permission.

Figure 1.7 The distribution of beak depth of the Medium Ground Finch (*Geospiza fortis*) on Daphne Major, Galápagos Islands, in 1976 before a drought (n = 751). After Grant (1986).

Figure 1.8 A single hypothetical trait in a sample of 1000 individuals is subjected to *truncation selection*. (a) The histogram of trait values for these individuals before selection is shown in blue (mean $= -0.02$, variance $= 0.96$). (b) Only individuals with trait values greater than -1.5 (n = 921) survived selection. The trait distribution after selection is shown in black. Selection has shifted the trait mean and contracted its variance (mean = 0.11, variance = 0.75). Statistical values are
$s = \bar{z}^* - \bar{z} = 0.13; (P^* - P)/P = -0.22; (P^* - P + s^2)/P = -0.21$.

Figure 1.9 Hypothetical examples of selection acting on normally-distributed trait distributions. Trait distributions are shown in blue before selection and in black after

selection. (a) An upward shift in mean with little change in variance; $\bar{z} = 0.00, P = 1.00, \bar{z}^* = 0.02, P^* = 0.96$. (b) a contraction in variance with no shift in mean; $\bar{z} = 0.00, P = 1.00, \bar{z}^* = 0.02, P^* = 0.80$. (c) An upward shift in mean with a contraction in variance; $\bar{z} = 0.00, P = 1.00, \bar{z}^* = 0.20, P^* = 0.80$. (d) An expansion of variance with no shift in mean; $\bar{z} = 0.00, P = 1.00, \bar{z}^* = 0.02, P^* = 1.33$.

Figure 1.10 Scatterplots plots showing the equivalence between covariance and the selection differential, *s*. The sample of 100 individuals in these plots were drawn from the trait and fitness distributions, $p(z)$ and $w(z)$, used in Fig. 1.8c. (a) Relative fitness as a function of trait value, z: $\bar{z} = -0.13, P = 0.98, \overline{w} = 0.97, Cov(w, z) = 0.21, r(w, z) = 0.81$. (b) Relative fitness as a function of squared trait values, z^2: mean $z^2 = 0.99, Var(z^2) = 0.98, Cov(w, z^2) = -0.17, r(w, z^2) = -0.46$.

Figure 1.11 Diagram of a crawling snake showing how the body pushes against points in the environment. Contractions of musculature in particular segments of the body (black) produce the forces that move the snake forward. From (Jayne 2020) with permission.

Figure 1.12 Distributitons of body and tail vertebral counts in the garter snake *T. radix* before and after selection. The samples before selection (n = 143) are standardized to zero means. In the samples after selection, the vertebral count of each individual is weighted by relative crawling speed. (a) Distribution of body vertebral counts before selection. (a) Distribution of tail vertebral counts before selection. (a) Distribution of body vertebral counts after selection. (a) Distribution of tail vertebral counts after selection.

Figure 1.13 Distributions of beak depth measurements before and after selection on the Daphne Major population of *Geospiza fortis*. (a) The distribution in 1976, before selection (n = 751). (b) The distribution in 1978, after a drought killed many birds (n = 90 survivors). Data from Boag and Grant (1984); after Grant (1986).

Figure 1.14 Distributions of standardized changes in means and variances. (a) Distribution of estimates of the standardized change in mean, $(\bar{z}^* - \bar{z})/\sqrt{P}$, n = 262. After Endler (1986). (b) Distribution of estimates of the standardized change in variance, $(P^* - P)/P$, n = 330. After Endler (1986). The red vertical line shows the transition from negative to positive change in variance. (c) Selection differential, *s*, illustrated as normal distributions after selection with mean shifted towards higher values. Line widths represent frequency in Endler's histogram; before selection (blue, with unit standard deviation and zero mean) and after selection (black). (d) Standardized change in variance, $(P^* - P)/P$, illustrated as normal distributions after selection with variance contracted or expanded. Line widths represent bin frequencies in Endler's histogram.

Figure 1.15 Distribution of estimates of the standardized change in variance, corrected for the effects of directional selection, showing that the predominant effect of selection is to contract variance. The red vertical line shows the transition from negative to positive change in variance. (a) Distribution of estimates of the standardized change in variance, $(P^* - P + s^2)/P$, n = 330. After Endler (1986). (b) Standardized change in variance, $(P^* - P + s^2)/P$, illustrated as normal distributions after selection with variance contracted or expanded. Line widths represent bin frequencies in Endler's (1986)

histogram, before (blue, with unit standard deviation and zero mean) and after selection (black).

Figure 2.1 Number of tail vertebrae as a function of number of body vertebrae in a sample of 143 newborn garter snakes (*Thamnophis radix*). The two counts are not demonstrably correlated in this sample ($r = 0.07$).

Figure 2.2 Two traits in a hypothetical sample of 100 individuals are subjected to truncation selection. (a) A scatter plot trait values for these individuals before selection is shown in blue, along with the sample's 95% confidence ellipse (the contour line within which 95% of the observations are expected to occur). (b) Only individuals with trait values greater than -1.0 for both traits survived selection ($n = 81$). The scatter plot of the sample after selection is shown in black along with its confidence ellipse. Selection has shifted the trait means upwards and contracted both variances, the covariance, and the correlation, although the latter effect is slight.

Figure 2.3 Changes in hypothetical bivariate trait distributions induced by selection. All of the distributions are normal before and after selection; 95% confidence ellipses are shown before selection (blue) and after selection (black). The position of bivariate means is shown with crosses. (a) Contractions in both variances with no shift in mean. (b) Contractions in both variances with an increase in the bivariate mean, $\bar{\boldsymbol{z}} = (0 \;\; 0)^{\mathrm{T}}$, where the superscript T denotes transposition that converts a row vector into a column vector. (c) Contractions in both variances and covariance with no shift in mean. (d) Contractions in

both variances and covariance with an upward shift in mean. (e) Substantial contractions in both variances and covariance with no shift in mean. (f) Substantial contractions in both variances and covariance with an upward shift in mean.

Figure 2.4 Large samples from two bivariate normal distributions of two traits, one with no trait correlation and the other with a strong positive correlation. (a) Above.- a 2-dimensional scatter plot of the individuals sampled from a distribution with no correlation: $(\bar{z}_1 = 0.0, \bar{z}_2 = 0.0, P_{11} = 1.0, P_{22} = 1.0, P_{12} = 1.0, r = 0.0)$. Below.- a 3-dimensional view of the probability distribution with no correlation. (b) Above.- a 2-dimensional scatter plot of the individuals sampled from a distribution with a strong positive correlation: $(\bar{z}_1 = 0.0,\ \bar{z}_2 = 0.0, P_{11} = 1.0, P_{22} = 0.9, P_{12} = 1.0, r = 0.9)$. Below.- a 3-dimensional view of the probability distribution with a strong positive correlation.

Figure 2.5 Histograms of selection linear gradients and differentials paired with frequency distributions that portray the magnitude of effects on means. (a) Histogram of the absolute values of directional selection differential estimates, s_i; 746 values from Kingsolver et al (2001) database. Three values greater than |2| are not included. (b) Shifts in mean corresponding to the directional selection differentials in Fig. 2.5a. Shifts corresponding to the five bins on the right-most side of the distribution (0.05-0.45) are shown in black and account for 92% of the observations. (c) Histogram of the absolute values of directional selection gradient estimates, β_i; 992 values from Kingsolver et al (2001). Three values for s_i greater than |2| were not included. (d) Shifts in mean corresponding to the directional

selection gradients in Fig. 2.5c. Shifts corresponding to the five bins on the right-most side of the distribution (0.05-0.45) are shown in black and account for 90% of the observations.

Figure 2.6 Histograms of selection nonlinear gradients and differentials paired with frequency distributions that portray the magnitude of effects on variances. (a) Histogram of nonlinear selection differential estimates, $C_i = (P_i^* - P_i + s_i^2)/P_i$; 220 values from the Kingsolver et al. (2001) database. Five values greater than |2| are not included. The vertical red line separates the distribution into negative and positive estimates. (b) Shifts in variance corresponding to the nonlinear selection differentials shown in Fig. 2.5e. Shifts corresponding to the four most populated bins in the center of the distribution (-0.15 to 0.15) are shown in black and account for 78% of the observations. (c) Histogram of nonlinear selection gradient estimates, γ_{ii}; 653 values from the Stinchcombe et al. (2008) database, after deleting 7 values of $\gamma_{ii} > 2$ and 4 values < -2. (d) Shifts in variance corresponding to the nonlinear selection gradients shown in Fig. 2.6g . Shifts corresponding to the 16 most populated bins in the center the γ-distribution (-0.4 to 0.4) are shown in black and account for 86% of the observations.

Figure 3.1 Examples of individual selection surfaces, ISSs, showing their effects on trait distributions. The statistics of the trait distributions before selection (blue), $p(z)$, and after selection (black), $p^*(z)$, are given in Fig. 1.8. The ISS, $w(z)$, is shown as an orange curve. (a) Directional selection. The ISS is a linear function, $w(z) = \alpha + \beta z, \alpha = 1, \beta = 0.2$. The orange line has been shifted down 0.3 units for graphic effect. (b) Stabilizing selection. The ISS is a Gaussian function with $\theta = 0, \omega = 4. \theta$. (c) Directional and stabilizing selection.

The ISS is a Gaussian function with $\theta = 0, \omega = 4$. (d) Disruptive selection. The ISS is a Gaussian function with $\theta = 0, \omega = -4$. The orange curve has been shifted down 0.8 units for graphic effect.

Figure 3.2 The directional selection gradient, β, as the weighted average of first derivatives of the ISS. The ISS is the orange curve; the trait distribution before selection, $p(z)$, is shown in blue. The first derivatives of the ISS for $z = -1$ is shown as the slope of the black, straight line segment superimposed on the ISS. The average of all such slopes, weighted by $p(z)$, is the directional selection gradient, β, shown as the slope of the red line segment. In this illustration, the ISS is a Gaussian function ($\theta = 0, \omega = 1$) and $p(z)$ is a normal distribution ($\bar{z} = -0.5, P = 1$).

Figure 3.3 The nonlinear selection gradient, γ, as the weighted average of second derivatives of the ISS. The ISS is the orange curve, $w(z)$; the trait distribution before selection, $p(z)$, is shown in blue. The first derivative of the ISS is the yellow curve. A first derivative of this yellow curve (which is the second derivative of the ISS) at $z = -1.5$ is shown as as a black line segment superimposed on the yellow curve. The average of all such slopes, weighted by the trait distribution, is the nonlinear selection gradient, $\gamma = -0.4375$, shown as the slope of the red line segment. In this illustration, the ISS is a Gaussian function ($\theta = 0, \omega = 1$) and $p(z)$ is a normal distribution ($\bar{z} = -0.5, P = 1$).

Figure 3.4 Linear and quadratic approximations to the ISS in a hypothetical example. Relative fitness, $w(z)$, is a function of trait value, z. (a) A linear fit to the data (Fig. 1.9)

using (3.02), $\alpha = 1, \beta = 0.21 \pm 0.02$ s.e. (b) A quadratic fit using (3.03), $\alpha = 1, \beta = 0.20 \pm 0.01$ s.e., $\gamma = -0.12 \pm 0.02$ s.e. (c) The actual ISS is a Gaussian function (3.8), shown in orange, $\theta = 1, \omega = 4$. The data points were generated by taking a random sample of trait values, z, from a normal distribution ($\bar{z} = 0, P = 1$). Those trait values were used in conjuction with the specified Gaussian function to produce corresponding, expected values of $w(z)$. Values of ε were drawn from a normal distribution (mean = 0, variance = 0.01) and added to expected value of w to produce the points in the figure (n = 100).

Figure 3.5 Selection on germination timing in Spring Blue-eyed Mary (*Collinsia verna*) in two study years (after Kalisz (1986)**.** Distributions of germination dates are shown before (blue) and after selection (black). The scores for germination date represent census periods lasting 7 or 10 days. Quadratic approximations to the ISS are shown in orange. (a) For the 1982 sample (n = 2,580 individuals that germinated and bore fruit), the ISS approximation is $w(z) = 1 + \beta z + \frac{1}{2}\gamma z^2$, where $\beta = -0.198$ *** and $\gamma = 0.014$ *ns* (*** denotes $P < 0.0001$ and *ns* denotes $P > 0.05$). Each of the six census periods lasted 10 days. (b) For the 1983 sample (n = 2,440 individuals that germinated and bore fruit), the ISS approximation is $w(z) = 1 + \beta z + \frac{1}{2}\gamma z^2$, where $\beta = -0.079$ * and $\gamma = 0.010$ *ns* (* denotes $P < 0.05$). Each of the seven census periods lasted 7 days.

Figure 3.6 A hypothetical example in which a quadratic approximation to the ISS is misleading in shape. The sample before selection is shown as a blue curve, a normal distribution with a mean of zero and a standard deviation of 1. The actual ISS, which exerts truncation selection, is shown in orange. The sample after selection is shown in black. The quadratric approximation to the ISS is shown as a black curve. This curve was estimated by

fitting a quadratic regression to a sample of 1000 individuals drawn from the normal distribution before selection and assigned relative fitnesses according to the truncation-function ISS. Although the black curve gives a poor idea of the ISS, it does give a good estimate of the selection gradients ($\beta = 1.62 \pm 0.04$ s.e., $\gamma = 1.79 \pm 0.07$ s.e.). After Schluter (1988).

Figure 3.7 An example of a cubic spline approximation to an unknown ISS. The solid black curve is a cubic spline of overwinter survival of male song sparrows (n =152) as a function of morphological measurements (Principal component 2). The dashed curves show $\pm$ 1 standard error of the function, estimated by bootstrapping. The crosses at the top and bottom show the absolute fitness and trait values of males that did and did not survive winters. Fitness is not normalized by dividing by its mean, as in other ISSs that we have depicted. From Schluter (1988) with permission.

Figure 3.8 The directional selection gradient, β, as the first derivative of the AL, evaluated at the trait mean before selection, $\bar{z} = -0.5$. The AL is shown as a red Gaussian curve with an optimum $\theta = 0$ and width parameter $\Omega = 2$. The directional selection gradient is shown at two sites connected by a dashed vertical line: at the trait mean of $z = -0.5$, where it is shown as a red line segment, and at the point of evaluation on the AL, where it is shown as a black line segment. Other conventions as in Fig. 3.3.

Figure 3.9 Gaussian ISSs and their corresponding Gaussian ALs for a range of values of ω. The blue curve shows a normal trait distribution before selection, $p(z)$, with a mean of 0 and a variance $P = 1$. The wide orange curves show the individual selection surfaces for

$\omega = 99$ (at the top), 49, 9, and 4 (at the bottom). The narrow red curves show the corresponding adaptive landscapes with width parameters $\Omega = \omega + P = 100$, 50, 10, and 5.

Figure 3.10 Gaussian approximations to quadratic individual selection surfaces (ISSs). Quadratic ISSs are shown as black curves and their Gaussian approximations are shown as orange curves. Expression (3.11) was used to approximate ω from γ. Optimum or pessimum of each quadratic surface set at zero. When $\omega = 0.5$ or -0.5 the approximation is so close that the quadratic curves are barely visible. (a) Gaussian approximations of stabilizing quadratic selection curves. From the top curve to the lowest, $\gamma(\omega)$ values are $-0.01(100)$, $-0.1(10)$, $-0.5(2)$, $-1(1)$, and -2 (0.5). (b) Gaussian approximations of disruptive quadratic selection curves. From the lowest curve to top, $\gamma(\omega)$ values are $0.01(-100)$, $0.1(-10)$, $0.5(-2)$, $1(-1)$, and 2 (-0.5).

Figure 3.11 Estimated movements of optimal laying date in *Parus major*. The main characteristics of the best fitting model are shown in the panel on the right: an estimated Gaussian ISS (solid curve) with an optimum that fluctuates about a stationary position and a width ($\sqrt{\omega} = 20.55$ days) that is substantially larger than the width ($\sqrt{P} = 5.35$ days) of the average within-year distribution of laying date, z (dashed curve). The panel on the left shows the time series for the estimates of the optimum, θ_t (solid line) with 95% credible interval (dashed lines) and mean laying date each year, z (dots). The yearly dates of peak nestling food (caterpillar) biomass (faint dotted line) are shown in the upper portion of the

panel. Yearly peaks prior to 1985 were estimated from temperature data and the 95%-prediction interval is shown (shading). From Chevin et al. (2015) with permission.

Figure 3.12 Histograms of selection gradients paired with frequency distributions that portray corresponding selection surfaces and the magnitude of effects on means and variances. Trait distributions before and after selection are shown in blue and black, respectively. (a) Histogram of the absolute values of directional selection gradient estimates, β; 992 values from Kingsolver et al. (2001). (b) Shifts in mean corresponding to the directional selection gradients in Fig. 3.8a. Shifts corresponding to the four bins on the right-most side of the distribution (0.05 - 0.45) are shown as black curves whose widths correspond to bin frequency. Orange curves show the fitness functions (ISSs) corresponding to those 4 bin categories, with widths corresponding to bin frequency. (c) Histogram of nonlinear selection gradient estimates, γ; 653 values from the Stinchcombe et al. (2008) database, after deleting 7 values of $\gamma > 2$ and 4 values < -2. (d) Shifts in variance corresponding to the nonlinear selection gradients shown in Fig. 3.8c . Shifts corresponding to the 16 most populated bins in the center the γ distribution (-0.4 to 0.4) are shown as four black curves (accounting for 86% of the observations) with width representing four bin category frequencies. Orange curves show the fitness functions (ISSs) corresponding to those 4 bin categories, with widths corresponding to bin category frequency.

Figure 3.13 Comparison of univariate variance- and mean-standardized directional selection gradients on arithmetic and logarithmic trait scales. Distributions of absolute values are shown (240 estimates are shown from 38 studies). Open bars denote results not significantly different from zero; shaded bars show significant results. (a) Distribution of variance-standardized selection gradients (9 estimates larger than 1.0 are not shown). (b) Distribution of log_{10}(variance-standardized selection gradients). (c) Distribution of mean-standarized selection gradients (101 estimates larger than 2.0 are not shown). (d) Distribution of log_{10} (mean-standarized selection gradients). After Hereford et al. (2004).

Figure 3.14 Histogram of distances of the phenotypic mean from the intermediate optimum, θ, in natural populations, with blue curves portraying the most frequent values of those distances. (a) Values were calculated using (3.12) with paired values of negative γ and absolute values of β from the Stinchcombe et al. (2008) database (n = 339, dropping two values greater than 50). Distance to the optimum is measured in units of within-population phenotypic standard deviation before selection. The median distance value is 0.906. (b) The orange curve shows the most frequent value of γ with a negative value in the histogram shown in Fig. 3.8c (bin centered at $\gamma = -0.025$ with a count of 80). The optimum, θ, is shown with a vertical dash-dot line. The blue curves show $p(z)$ with trait means at distances of -0.5, -1.5, -2.5, -3.5 and -4.5 from θ, corresponding to the first 5 bins in the histogram with relative frequencies portrayed with line widths. The positions of trait means are shown with vertical dashed lines.

Figure 4.1 Bivariate stabilizing selection represented as a convex selection surface. Relative fitness, $w(\boldsymbol{z})$, corresponds to points on the surface as a function of the values of two traits z_1 and z_2. A contour representation of the surface is projected onto the z_1 x z_2 plane with contours at increments of 0.2 in relative fitness. This surface is quadratic with $\alpha = 1, \beta_1 = 0.22,\ \beta_2 = -0.08, \gamma_{11} = -0.31, \gamma_{22} = -0.18,$ and $\gamma_{12} = 0.07$.

Figure 4.2 Contour and confidence ellipse portrayal of a selection surface. The optimum of the surface is at $z_1 = 0$ and $z_2 = 0$. The thin orange ellipses represent equal values of relative fitness at increments of 0.2. The bold orange ellipse represents the analog to a 95% confidence ellipse. See text for more details.

Figure 4.3 Various forms of Gaussian selection and their effects on bivariate trait distributions. Ellipses comparable to 95% confidence ellipses are shown for Gaussian ISSs (orange). Phenotypic trait distributions are bivariate normal before (blue 95% confidence ellipses) and after selection (black 95% confidence ellipses). Bivariate means, variances and covariances, before and after selection, are given in the caption for Fig. 2.3. Parameters for the ISSs are the same in Fig. 2.3. The relationshiop of the γ-matrix to the ω-matrix will be discussed in section 4.4. In the left-hand panel, the trait distribution experiences nonlinear selection, but no directional selection. In the right-hand panel, directional selection has been added by shifting the position of the optimum, θ. (a) Symmetrical stabilizing selection contracts the trait variance without shifting the mean. (b) When the optimum is displaced from the trait mean in both directions, the trait distribution after selection shifts towards the optimum. (c) Positive correlational selection is reflected in the

positive inclination of the *ISS*-ellipse. When this ellipse is aligned with the *P*-ellipse (blue), the inclination of the P^*-ellipse (black) is not changed by selection. (d) Displacement of the optimum from the trait mean, combined with aligned γ- and *P*-matrices, shifts the trait distribution towards the optimum. (e) Nonalignment of the γ- and *P*-matrices causes a dramatic change in trait covariance (compare *P*- and P^*-ellipses). (f) Nonalignment of the γ- and *P*-matrices, combined with a displaced optimum, shifts the trait distribution towards the optimum.

Figure 4.4 Hypothetical quadratic ISSs for two traits. Peaks are denoted with a + sign and depressions with a – sign. Dotted lines represent the canonical (principal) axes of the surface. Trait means are denoted with μ and phenotypic standard deviation with σ. Despite the differences in the appearance of these surfaces, the values of the elements in their γ-matrices are only slightly different. See Phillips and Arnold (1989) for details. From Phillips and Arnold (1989).

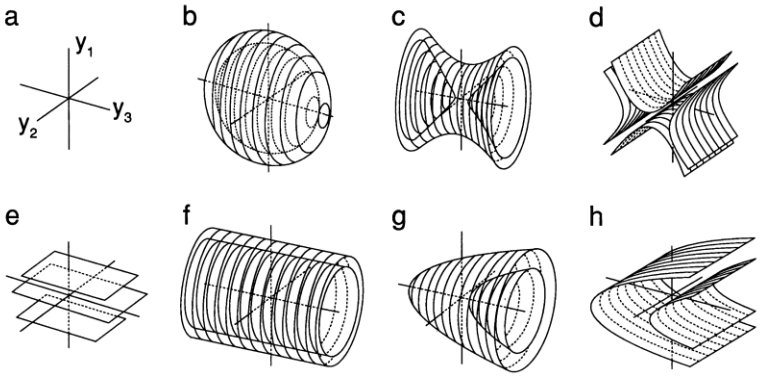

Figure 4.5 Quadratic selection on three traits. The three trait canonical axes are shown in a. Fitness is a fourth axis. All points on each surface have the same fitness. Two same-fitness surfaces are shown in each case. In b and c, maximum fitness is at the origin. In d and f maximum fitness is a line and in e it is a plane. (a) Axis labels. (b)

Stabilizing selection on all three traits $(\lambda_1, \lambda_2, \lambda_3)$ = (-,-,-). (c) Stabilizing selection on y_1 and y_2, disruptive selection on y_3 (-,-,+). (d) Stabilizing selection on y_1, no selection on y_2, disruptive selection on y_3 (-,0,+). (e) Stabilizing selection on y_1, no selecton on y_2 or y_3 (-,0,0). (f) Stabilizing selection on y_1 and y_2, no selecton on y_3 (-,-,0). (g) Stabilizing selection on y_1 and y_2, strong directional selection on y_3 ($\theta_3 > 0$; center of system is undefined, the surface is a rising ridge) (-,-,0). (h) Stabilizing selection on y_1, no selection on y_2, strong directional selection on y_3 (-,0,0). From Phillips and Arnold (1989).

Figure 4.6 A Gaussian ISS (a) and corresponding Gaussian AL (b) are similar in configuration if stabilizing selection is weak, as in this example: Gaussian ISS with $\boldsymbol{\theta} = (0\ \ 0)^{\mathrm{T}}$ and $\boldsymbol{\omega} = (5\ \ 2.5, 2.5\ \ 5)$ and the corresponding Gaussian AL with $\boldsymbol{\Omega} = (6\ \ 2.5, 2.5\ \ 6)$, where $\boldsymbol{P} = (1\ \ 0, 0\ \ 1)$.

Figure 4.7 Contour plot portrayals of weak bivariate Gaussian ISSs and their corresponding adaptive landscapes. In each figure the optimum is at $z_1 = 0$ and $z_2 = 0$, and $\boldsymbol{P} = (1\ \ 0, 0\ \ 1)$. Eigenvectors are shown as dashed lines. Matrix representations are superimposed on each surface. (a) An ISS with equally strong stabilizing selection on each trait with no correlational selection. Contours show equal values of relative fitness, $w(\boldsymbol{z})$. (b) The AL corresponding to Fig. 4.7a. Contours show equal values of average absolute fitness, $\overline{W}$. (c) An ISS with equally strong stabilizing selection on each trait and strong correlational selection, $r_\omega = 0.9$. (d) The AL corresponding to Fig. 4.7c.

Figure 4.8 Quadratic approximation of a crawling speed performance surface in the garter snake *T. radix*. Body and tail vertebral counts are shown, respectively on the x- and y-axes. The 3-dimensional surface (a) and the contour surface (b) were drawn using selection gradients estimated by linear and quadratic regression. Eigenvectors are shown as dashed lines. The stationary point, calculated using (4.5e), is at the intersection of the eigenvectrors, near the center of each bivariate plot. The slope of the leading eigenvector is approximately +1 while the slope of the trailing eigenvector is approximately -1.

Figure 4.9 Viability selection as a function of coloration pattern and antipredator behavior in the garter snake *T. ordinoides*. Survival in the field is shown as a function of reversals (the tendency to reverse directions during simulated predation exposure in the laboratory) and stripe (overall stripedness of the color pattern). Contours show relative fitness (survival) as a quadratic function of reversals and stripe. Eigenvectors are shown as dashed lines. Selection is stabilizing (concave) along the leading eigenvector (I) and disruptive (convex) along the second eigenvector (II). (a) The bivariate sample before selection (n = 646). (b) The bivariate sample after selection (n = 101). (c) Surface plot of the quadratic selection function. From (Brodie 1992) with permission.

Figure 4.10 Comparison of multivariate variance- and mean-standardized directional selection gradients on arithmetic and logarithmic scales. Distributions of absolute values are shown (340 estimates are shown from 38 studies). Open bars denote results not significantly different from zero; shaded bars show significant results. (a) Distribution of variance-standardized selection gradients (14 estimates larger than 1.0 are not shown). (b)

Distribution of log_{10}(variance-standardized selection gradients). (c)Distribution of mean-standarized selection gradients (78 estimates larger than 1.5 are not shown). (d) Distribution of log_{10} (mean-standarized selection gradients). After Hereford et al. (2004).

Figure 4.11 Survival probability in human infants as a function of birth mass (pounds) and gestation period (days). (a) Fitness contours (increments of 0.5) describe a dome rising steeply from the lower left to a broad plateau. The size of the symbols (filled circles) is proportional to probability of survival. The directions (a_1, a_2) used to approximate the surface are labeled #1 and #2. (b) A three dimensional portrayal of the surface. From Schluter and Nychka (1994) with permission.

Figure 4.12 Thin-plate spline visualizations of the mate choice surface in crickets (*Teleogryllus commodus*), using call eigenvectors that demonstrated significant stabilizing selection as axes: (a) $\boldsymbol{m_6}$ and $\boldsymbol{m_5}$, (b) $\boldsymbol{m_4}$ and $\boldsymbol{m_5}$, and (c) $\boldsymbol{m_6}$ and $\boldsymbol{m_4}$. The vertical axes are proportional to numbers of females attracted using particular combinations of call parameters. From Bentsen et al. (2006) with permission.

Figure 5.1 Galton's data shown as a human offspring versus parent plot of height in a British population. Each point represents a combination of average offspring (n = 928) and average parental values (n = 205 sets). The size of each point is proportional to the sample size of that trait combination. The dashed line shows perfect inheritance. The solid line is a least-squares regression. From Arnold (1994).

Figure 5.2 The distribution of phenotypic values as the sum of underlying genotypic distributions, showing that the sum rapidly converges on a normal distribution. In this example, each of 20 genes contributes to a slightly to moderately trimodal distribution in which the value of the heterozygote is 0 and the values of the two homozygotes are symmetrical about zero with an absolute value drawn from a normal distribution (mean = 0, standard deviation = 0.75). The environmental variances of the three genotypes at a locus are each 0.04, and the three genotypes occur at a 1:2:1 ratio. The gray curves show the accumulated frequency distributions of 1, 2, 3 … 19 loci. The blue curve shows the accumulated distribution when the trimodal contributions of 20 loci are summed. For an animated version of this figure see https://phenotypicevolution.com/?p=338

Figure 5.3 Hypothetical plots of offspring versus midparent values. Each plot portrays a sample of 100 offspring-parent values sampled from a bivariate normal distribution. (a) In the parametric distribution, $h^2 = 0$. In the sample, $h^2 = 0.03 \pm 0.09$ s. e. (b) In the parametric distribution, $h^2 = 0.5$. In the sample, $h^2 = 0.59 \pm 0.09$ s. e. (c) In the parametric distribution, $h^2 = 0.9$. In the sample, $h^2 = 0.85 \pm 0.05$ s. e.

Figure 5.4 Song sparrow (*Melospiza melodia*) offspring resemble their biological parents but not their foster parents. (a) Beak depth of midoffspring as a function of the beak depths of their true (biological) parents ($y = -0.01 + 0.98\,x,\ r^2 = 0.496$). (b) Beak depth of midoffspring as a function of the beak depths of their foster parents ($y = 6.86 - 0.18\,x,\ r^2 = 0.011$). After Smith and Dhondt (1980).

Figure 5.5 Offspring versus parent heritability plots in the garter snake *Thamnophis elegans* (inland population). (a) The average body vertebral count of daughters is plotted against the mother's count: n = 151, corresponding to an estimated genetic variance of 8.17 ± 1.70 s. e., $h^2 = 0.54 \pm 0.10$ s. e. (b) The average tail vertebral count of daughters is plotted against the mother's count: n = 120, corresponding to an estimated genetic variance of 8.16 ± 1.73 s. e., $h^2 = 0.48 \pm 0.10$ s. e. Data from Arnold and Phillips (1999).

Figure 5.6 Estimates of the proportion of additive genetic variance in human height explained by genic regions of each chromosome using a joint analysis. The boundaries of protein-coding genes (genic regions) are defined as $\pm$50 kb of the 3' and 5' UTRs. After Yang et al. 2011b.

Figure 5.7 Histogram of a large sample (n = 580**) of heritability estimates for morphological characters in vertebrate and invertebrate animals.** Note that estimates outside the parameter range ($0 \leq h^2 \leq 1$) are possible with some estimation procedures. Mean = 0.47, median = 0.44, variance = 0.10. Based on data in Mousseau & Roff (1987), courtesy of D. Roff.

Figure 5.9 Distributions of bristle counts among chromosome substitution lines derived from a single natural population of *Drosophila melanogaster*. (a) Variation in abdominal bristle number from chromosome 2 substitution lines. (b) Variation in abdominal bristle number from chromosome 3 substitution lines. (c) Variation in sternopleural bristle

number from chromosome 2 substitution lines. (d) Variation in sternopleural bristle number from chromosome 3 substitution lines. After Mackay and Lyman (2005).

Figure 5.10 A flowchart view of mutation-selection balance. Recombination converts hidden variation into expressed variation by decreasing correlations between loci, while stabilizing selection has the reverse affect (center). Mutation does not alter the hidden variation but contributes directly to the expressed genetic variation, while stabilizing selection depletes expressed variation (left). At equilibrium, the flow out of expressed variation into hidden variation equals the flow into expressed variation, regardless of the rate of recombination of the loci. After Lande (1976).

Figure 5.11 Three different candidate distributions for mutational effects. Each of these examples has a mean of zero and a variance of about 0.05: Gaussian distribution (dashed line), reflected exponential (Laplace) distribution (dotted line), and reflected gamma distribution (solid line). After Bürger (2000).

Figure 5.12 Curves showing the hypothetical distribution of breeding values before selection (blue; $G = 0.400$) and after selection ($G^* = 0.368$), when stabilizing selection is relatively strong, ($\gamma = -0.2$) and $\beta = 0$. In an equilibrium population, mutation would restore variation in the next generation.

Figure 5.13 Pooled distributions of additive and dominance effect sizes of QTLs (n =144**) for abdominal and sternopleural bristle numbers in *Drosophila melanogaster*.** (a)

Distribution of additive effect sizes shown as a ratio of estimated additive effect to additive genetic standard deviation, $/\sqrt{G}$. (b) Distribution of dominance effect sizes, d/a . After Dilda & Mackay (2002).

Figure 6.1 Alternative genotype-phenotype maps for multiple traits. (a) Each trait affected by a single, private gene. (b) Each trait affected by multiple private genes. (c) Each trait affected by multiple non-private genes, no pleiotropy. (d) Each trait affected by multiple non-private genes, no pleiotropic. (e) Each trait affected by multiple non-private genes, with pleiotropy.

Figure 6.2 Examples of genetic covariance estimated from offspring-parent plots in the garter snake *T. elegans* (inland population). (a) The average tail vertebral count of daughters as a function of mother's body vertebral count, n = 154. (b) The average body vertebral count of daughters as a function of mother's tail vertebral count, n = 117. The estimate of genetic covariance based on both sets of data is 3.78 ± 1.67s. e. Data from Phillips and Arnold (1999).

Figure 6.3 Hypothetical bivariate samples of genetic values (n = 100**) from bivariate normal distributions with genetic correlations, r_g , of (a) 0, (b) 0.8, and (c) -0.8.** Sample 95% confidence ellipses for the bivariate mean are shown. Straight lines show the eigenvectors for the matrices shown in each figure, rather than each sample.

Figure 6.4 Prevalence of genetic correlation between morphological traits. The histogram summarizes 1210 estimates from 38 species. Frequency is shown as a percent of observations. Mean $= 0.47 \pm 0.009$s. e. After Roff (1997).

Figure 6.5 Correlational selection can create and maintain linkage disequilibrium. In this hypothetical example, the *A* locus affects the color of the head of a grasshopper, so that *A_* (*AA* and *Aa*) grasshoppers have green heads and *aa* grasshoppers have brown heads. The *B* locus affects the color of the body, so that *B_* (*BB* and *Bb*) grasshoppers have green bodies and *bb* grasshoppers have brown bodies. Correlational selection acting on this inheritance scheme can produce linkage disequilibrium. Suppose, for example, that color-matched grasshoppers are favored in the population because they are harder for predators to detect. In contrast, color miss-matched grasshoppers stand out against both green and brown backgrounds and fall prey to predators on both backgrounds. This selection scheme creates linkage disequilibrium between the two loci such that the haplotypes *AB* and *ab* are disproportionally represented in the population. This disequilibrium is expressed as a genetic correlation between colors in the head and body.

Figure 6.6 Landmarks on the wing of *Drosophila melanogaster*. From Mezey and Houle (2005) with permission.

Figure 6.7 Dimensionality analysis of the G-matrix for 24 landmark traits on the wing of male *Drosophila melanogaster*. Solid circles show the eigenvalue estimates for each eigenvector. After Mezey and Houle (2005).

Figure 6.8 The distribution of new mutational effects on two traits from a particular locus can be represented as a cloud of values. Samples of 25 hypothetical alleles drawn from bivariate normal distributions are plotted along with the 95% confidence ellipses for the means. Axes inside each ellipse are eigenvectors (principal components). (a) A cloud of mutational effects with no correlation, $r_\mu = 0$. (b) A cloud of mutational effects with a strong positive correlation, $r_\mu = 0.9$. After Arnold et al. (2008).

Figure 6.9 Average wing shapes of 112 drosophilid species and 5 outgroup taxa. Each point show the aligned position of a single landmark site in one taxon. Inset shows the phylogeny of major drosophilid taxa. Grey diamonds denote outgroup taxa. From Houle et al. (2017) with permission.

Figure 7.1 The venom production and delivery module of a rattlesnake. (a) The resting positions of the venom gland, venom duct, maxillary bone, and fang in the head of the viper. (b) A biomechanical model for fang erection shown the resting and (c) erect position of the fang (15), and the 11 linked bones responsible for erecting the fang: maxillary (1), prefrontal (2), frontal (3), parietal (4), squamosal (5), palatine (8), pterygoid (9), ectopterygoid (10), and quadrate (11). From Klauber (1956) with permission.

Figure 7.2 The tongue projection mechanism of a plethodontid salamander. The tongue skeleton (black) is normally folded inside the body cavity but is projected forward during prey capture by contracted protractor muscles (dark red). Retractor muscles (light red),

attached to the tongue skeleton, run the full length of the body and attach to the pelvis. The contraction of these muscles pulls the tongue and attached prey back into the body. After Deban et al. (1997).

Figure 7.3 Courtship pheromone delivery during the tail-straddling walk of the salamander *Plethodon shermani*. The male (left) holds his mental gland over the female's head before slapping it across her nares and delivering a pheromone cocktail.

Figure 7.4 An African egg-eating snake (*Dasypeltis*) in the process of swallowing its prey. The lengths of 5 structural elements determine the maximal cross-sectional area of prey than can be ingested: width of the brain case (z_1), and the lengths of the supratemporal (z_2), quadrate (z_3), mandible (z_4), and mandibular symphysis (z_5). Based on Gans (1952), from Arnold (1983).

Figure 7.5 Path diagram showing causal relationships (paths with single arrowhead) between k morphological traits ($z_1, z_2, \cdots z_k$), two measures of performance (f_1 and f_2), and relative fitness (w). Double-headed arrows represent phenotypic covariances between traits, before selection. The covariances between the first and fourth traits and between the first and kth traits are labeled, respectively, P_{14} and P_{1k}. Ffrom Arnold (1983).

Figure 7.6 A path diagram showing multivariate linear performance and fitness gradients, $\boldsymbol{\beta}_f$ and $\boldsymbol{\beta}_w$, that relate trait values to performance and performance values to fitness. Column vectors of trait and performance values are denoted $\boldsymbol{z}$ and $\boldsymbol{f}$. The residual value of performance, unaccounted for by trait values, is denoted ε_f. Fitness and the residual

values of fitness, unaccounted for by trait values, are scalars and are denoted respectively as $w = w(\boldsymbol{z})$ and ε_w. From Arnold (2003).

Figure 7.7 A path diagram showing the multivariate linear ($\boldsymbol{\beta}_w$, a vector) and nonlinear ($\boldsymbol{\gamma}_w$, a matrix) performance gradients that related trait values to performance. Other conventions as in Fig. 7.5. From Arnold (2003).

Figure 7.8 Path diagram showing the multivariate linear ($\boldsymbol{\beta}_w$, a vector) and nonlinear ($\boldsymbol{\gamma}_w$, a matrix) fitness gradients that relate performance to fitness. Other conventions as in Fig. 7.5. From Arnold (2003).

Figure 7.9 Biomechanical models for the bite force of the lower jaw of the lizard *Tropidurus hispidus*. (a) The diagram illustrates three lever arm models that open (*c* and *d*, *a* and *d*) and close (*p* and *d*) the lower jaw. The small red circle denotes the fulcrum of the lever arms. (The suragular bone is not shown in this view of the skull and it participates in forming an outlever with the dentary). (b) The three polygons represent muscles that pull *c* (yellow), *a* (blue), and *p* (orange) upwards towards the top of the skull. The brown circle represents a prey item against which the lower jaw exerts bite force. Based on diagrams in Gröning et al. (2013) and Simon et al. (2019).

Figure 7.10 The bite force performance surface and contour plot for two eigenvectors of the γ-matrix ($\mathbf{m}_3$ and $\mathbf{m}_5$) in the lizard *T. hispidus*. (a) A quadratic surface fitted to relative bite force as a function of $\boldsymbol{m}_3$ and $\boldsymbol{m}_5$. (b) Relative bite force graphed as a function of $\boldsymbol{m}_3$ and

$\boldsymbol{m_5}$ (black dots) and contours (orange) are fitted to the data. The star indicates the position of the bivariate mean. From Simon et al. (2019).

Figure 8.1 Histogram of N_e estimates using the temporal genetic method (n = 144**).** Most estimates are for vertebrate and invertebrate animals. After Palstra and Ruzzante (2008).

Figure 8.2 Genetic drift causes the phenotypic mean of a lineage to undergo a random walk. In these simulations of 400 generations of genetic drift, the lineage trait mean, $\bar{z}$, is shown in units of within-population phenotypic standard deviation, $\sqrt{P}$. (a) The random walk of a single lineage of small effective size. The random walks of 100 replicates lineages are shown for small (b) and moderate sized (c) populations. The theoretical 99% confidence limits for the distribution of lineage means, based on (8.5), are shown as dotted blue curves. The deterministic trait mean is shown as a white line.

Figure 8.3 Distributions of lineage trait means under neutrality. Probability, $\Phi(\bar{z}_t)$, is plotted as a function of trait mean, $\bar{z}_t$. Each curve represents the distribution of lineage means after some number of elapsed generations, t. Additive genetic variance $= 0.4$ and $N_e = 1000$.

Figure 8.4 Divergence in trait means as a function of elapsed time. Divergence is measured as the difference between average trait values of an ancestral and a descendant population, in units of pooled phenotypic standard deviation. The solid lines are fitted regression lines. The slopes of those fitted lines are equivalent to $0.84\sqrt{P}$ per million generations. The

dashed lines show the 99% confidence ellipse for the data. (a) Arithmetic by log plot. (b) Log by log plot. From Estes and Arnold (2007).

Figure 8.5 A simulation of drift in 20 replicate populations for 10,000 generations. The blue lines show the theoretical 99% confidence limits for lineage trait means. The white line shows the expected average of lineage means as a function of time. The violet lines show the limits of phenotypic divergence that are observed on timescales less than 1 million generations (Estes and Arnold 2007; Uyeda et al. 2011), namely, less than ± 6 within-population phenotypic standard deviations, $6\sqrt{P}$.

Figure 8.6 A hypothetical phylogeny for three taxa ($\boldsymbol{a}, \boldsymbol{b}, \boldsymbol{c}$). The timescale is indicated at the right in generations.

Figure 8.7 Q_{ST} as a function of F_{ST} in a sample of 29 studies. Each study estimated the two variation measures for multiple traits in a single species. Average values across traits are indicated with solid circles. The range of Q_{ST} values across multiple traits sampled in each species is shown with open circles. The solid line shows $Q_{ST} = F_{ST}$. From McKay and Latta (2002) with permission.

Figure 8.8 Q_{ST} as a function of F_{ST} in a sample of 143 studies. Points representing different traits in the same study are included. The dashed red line shows $Q_{ST} = F_{ST}$. A fitted relationship between Q_{ST} and F_{ST} is shown as a solid black line. Dark and light gray areas show 50% and 95% posterior density intervals. From Leinonen et al. (2013) with permission.

Figure 9.1 Simulations of the drift of the bivariate trait mean for 2,000 generations. The effective population size is 500. The 95% confidence ellipses for the G-matrix is shown in solid blue. The 95% confidence ellipses for the dispersion of lineage means after 2,000 generations are shown in dotted blue. Evolutionary paths of the bivaraite trait mean are shown as thin black lines. The red dots show the position of the bivariate trait mean at generation 2,000. (a) Drift of a single lineage with no genetic correlation. (b) Drift of five replicate lineages with no genetic correlation. (c) Drift of one lineage with a genetic correlation of 0.9. (d) Drift of five replicate lineages with a genetic correlation of 0.9.

Figure 9.2 Dispersion of bivariate lineage means evolving by drift at various elapsed intervals from time zero. The 95% confidence ellipse for the G-matrix is shown as a solid ellipse. The 95% confidence ellipses for the dispersion of lineage means are shown in dotted blue. (a) Dispersion of bivariate means for replicate lineages with no genetic correlation. (b) Dispersion of bivariate means for replicate lineages with a genetic correlation of 0.9.

Figure 9.3 The evolution of body and tail vertebral counts in natricine snakes. (a) Phylogeny of *Thamnophis* species and three species in the sister genus *Nerodia* (adapted from de Queiroz et al. (2002). Diagrams on the right show numbers of body (solid box) and tail vertebrae (open box) for tip taxa. The scale bar in the top left equals 2% sequence divergence in mtDNA. (b) Dispersion of species means in bivariate vertebral count space, with superimposed axis of maximum divergence ($\boldsymbol{d}^*_{max}$). The dotted ellipse represents the

average of *G*-matrices from two populations of *T. elegans*. After Hohenlohe and Arnold (2008).

Figure 9.4 Visualization of the stepwise procedure for testing how well different aspects of the G-matrix account for trait divergence. (a) Comparison of direct and ML estimates of matrix size. The direct estimate of the *G*-matrix is shown as the large blue ellipse, based on the average *G*-matix for *T. elegans*. The ML estimate for size (Σ) is shown as the much smaller blue, gray-filled ellipse. (b) Comparison of the ML estimate for size (dashed blue, gray-filled ellipse) with the ML estimate of shape (ε, solid blue ellipse). (c) Comparison of the ML estimate for shape (dashed blue, gray-filled ellipse) with the ML estimate of orientation (φ, solid blue ellipse). (d) Estimates of orientation of $\boldsymbol{\omega_{max}}$ from growth rate in *T. elegans* (orange line) and from crawling speed in *T. radix* (orange line) plotted along with the direct estimate of $\boldsymbol{g_{max}}$ (dashed dark blue line) and $\boldsymbol{d^*_{max}}$ (solid black line, the tree-corrected version of $\boldsymbol{d_{max}}$). After Hohenlohe and Arnold (2008).

Figure 9.5 Variation ellipses contrast the patterns of mutational variation ($\boldsymbol{M_{hom}}$, $\boldsymbol{M_{het}}$), standing genetic variation ($\boldsymbol{G}$), and variation in divergence ($\boldsymbol{R}$) around each landmark. The *R*-matrix was estimated from the among-species variance in means and is equivalent to the *D*-matrix, discussed above. Matrices are scaled to the same size, so that areas of ellipses are relative to the total variance within each matrix. From Houle et al. (2017) with permission.

Figure 10.1 Response to selection as a regression problem. (a) A plot of hypothetical offspring trait values as a function of hypothetical mid-parental trait values, showing h^2, the slope of the regression line (heavy line). (b) Truncation selection acts so that one set of parents (points shown in black) becomes the actual parents of the next generation. Their trait mean is $\bar{z}^*$, whereas the mean of all potential parents (blue and black points) is $\bar{z}$. The vertical lines project the trait means before and after selection up to the regression, which yields the two expected offspring means (horizontal lines), and hence the expected response to selection.

Figure 10.2 Simulated response to selection in a set of replicate populations of finite size. In the simulations depicted here, 100 lineages of moderate size ($N_e = 500$) respond to very weak directional selection ($s = 0.01$) for 500 generations. The trajectories of the lineage means (shown in black) reflect both response to selection and drift. The deterministic response to selection is shown as a white line. The 99% confidence limits for the overall lineage mean are shown with dotted blue lines.

Figure 10.3 Response to deliberate selection on new mutations for bristle numbers in *D. melanogaster*. In each selected line, the 10 pairs with the most extreme trait scores were selected in a sample of 40 pairs in generations $1 - 64$. In generations $65 - 206$, the 10 pairs with the most extreme scores were selected from a sample of 20. (Upper panel) Three replicate high lines and three replicate low lines. (Lower panel) Two replicate high lines and three replicate low lines. From Mackay et al. (2005) with permission.

Figure 10.4 Landmark traits that were used to construct targets of deliberate selection in *D. melanogaster*. (Left) Full wing, showing the trait region. (Right) Detail of the trait region. D_1 is the distance between two upper points. D_2 is the distance between the two lower points. From Weber (1992) with permission.

Figure 10.5 Response to deliberate selection on angular traits in *D. melanogaster*. Response to selection for large D_1/small D_2 (circles) and to small D_1/large D_2 (squares), $\pm$ s.e. (vertical lines). Responses are shown as the angular difference from control lines. Realized heritabilities estimated from these selection responses were 0.12 ± 0.02 s.e. (up line) and 0.24 ± 0.02 s.e. (down line). After Weber (1992).

Figure 10.6 A contour plot of geographic variation in mean wing length in the Downy Woodpecker (*Dryobates pubescens*) in eastern USA. Contours were fitted with an iterative methodology. Contour interval is 1 mm, n = 1038 specimens, $P \approx 4$. From James (1970) with permission.

Figure 10.7 Graphical illustrations of the additive theory of reciprocal transplants between two environments (geographic sites). The phenotypic trait mean in each environment is the sum of a genotypic and an environmental part. Four cases are shown in the panels on the left side with phenotypic trait means shown as solid black dots. Genotypic parts are shown in blue and environmental parts are shown in orange. The geographic difference in trait means is shown as a solid black line ($\bar{z}_2 > \bar{z}_1$ in all cases). The results of transplants (dotted black lines) are shown on the right side with trait means in native environments

shown as solid circles and trait means in foreign environments shown as open circles. (a) The geographic difference in the trait mean is wholly genotypic: $\bar{g}_2 > \bar{g}_1$ and $\bar{e}_2 = \bar{e}_1$. (b) The geographic difference in the trait mean is wholly environmental: $\bar{g}_2 = \bar{g}_1$ and $\bar{e}_2 > \bar{e}_1$. On the right, the dotted transplant lines are hidden by the solid geographic line. (c) Cogradient basis for the geographic difference in the trait mean: $\bar{g}_2 > \bar{g}_1$ and $\bar{e}_2 > \bar{e}_1$. (d) Countergradient basis for the geographic difference in the trait mean: $\bar{g}_2 > \bar{g}_1$ and $\bar{e}_2 < \bar{e}_1$. See Berven et al. (1979) for an alternative graphical analysis.

Figure 10.8 Graphical summary of body size at first reproduction of female Wood Frogs (*Rana sylvatica*) reciprocally transplanted between lowland (L) and mountain (M) geographic sites. Graphical conventions as in Fig. 10.7. After Berven (1982).

Figure 10.9 Distribution of effect size of mutations fixed during a simulation study of evolution towards a new trait optimum. The proportion of observations is graphed as a function of effect size. After Orr (1999).

Figure 10.10 Inheritance of eye ball diameter in a cross between surface- and cave-dwelling populations of fish (*Astyanax*). Frequency is shown as a percent of observations. (a) Distributions of eye size in cave-dwelling (P_1, n = 30) and surface-welling (P_2, n = 30) populations and their hybrids (F_1, n = 30). (b) Eye size distribution in BC_2 (n = 142), a cross between P_2 and F_1. (c) Eye size distribution in BC_1 (n = 450), a cross between P_1 and F_1. (d) Eye size distribution in the F_2 (n = 702). After Wilkins (1971).

Figure 10.11 Theoretical means and variances of a quantitative trait in a cross between two parental populations according to the additive model of inheritance. Trait variance is graphed as a function of trait mean in parental populations and their derived hybirds. (a) An example case in which the variance in P_2 is greater than in P_1. (b) An example case in which the variance in P_1 is greater than in P_2. After Lande (1981).

Figure 10.12 Examples of the inheritance of quantitative traits in crosses between divergent parental populations. Graphical conventions as in Fig. 10.8. Thin vertical and hortizontal lines show $\pm$ 1 standard error. Standard errors for the trait means for the first five cases were small and are not shown. Trait meansurement is denoted as x. Standard errors (se) of n_2 and n_4 are the square roots of corresponding estimates of $Var(n_E)$. (a) Tomato, fruit weight (gm), $\log(x - 0.153)$, data from Powers (1942), scale from Wright (1968), $n_2 = 10.0 \pm 0.7\ se$. (b) *Astyanax*, eye diameter, x is an artibrary unit of measurement, data from Wilkins (1971), $n_2 = 5.9 \pm 0.4\ se$. (c) Maize, percent oil in kernels, $\log(x + 1.87)$, data from Sprague and Brimhall (1949), scale from Wright (1968)), $n_2 = 19.4 \pm 3.1\ se$. (d) Hawaian *Drosophila*, female head shape, arctan(head width/head length), data from Val (1977), scale from Templeton (1977), $n_2 = 9.4 \pm 3.6\ se$. (e) Goldenrod (*Solidago*), date of anthesis, date relative to August, from Goodwin (1944), $n_2 = 6.4 \pm 1.4\ se$. (f) Human, skin color, antilog (relectance at 685 $m\mu$), data from Harrison and Owen (1964), $n_4 = 4.6 \pm 3.3\ se$. Analysis and graphics after Lande (1981).

Figure 10.13 LOD scores for a hypothetical quantitative trait with evidence for QTLs on 4 chromosomes. In this hypothetical example, data were simulated for 250 backcross

progeny with 12 chromosomes, each 100 cM long, four of which are shown in the panels. See Lander and Bottstein (1989) for the details of the simulation. The dotted lines at $LOD = 2.4$ shows the required significance level to detect a QTL. The gray bars show one LOD support interval for the position of the QTLS (solid triangle). Outside this region, the odds ratio falls off by a factor of 10. The lines extending beyond the gray bars show two LOD confidence intervals. Maximum likelihood estimates of the phenotypic effect of the QTL are shown to the right of the thin lines. From Lander and Botstein (1989) with permission.

Figure 10.14 Results of a meta-analysis of largest QTL effect size and total variation explained in 52 QTL studies using inbred-line crosses and assays of 222 traits. Frequencies shown are counts. (a) Distribution of r^2 values for QTL of largest effect in each study. (b) Distribution of r^2 values for all QTLs detected in each study. After Lynch and Walsh (1998).

Figure 10.15 Relationship between the percent of phenotypic variation explained and the number of QTLs detected in the studies summarized in Fig. 10.14. After Lynch and Walsh (1998).

Figure 10.16 Genomic positions of 75 QTLs that affect growth in mice on each of 19 linkage groups. E and L denote effects on early and late growth respectively. Entries in parentheses affect early or late weight but not growth itself. From Cheverud et al. (1996) with permission.

Figure 10.17 The plate-spine functional complex in *Gasterosteus aculeatus*. C, cleithrum; D1, first dorsal spine; D2, second dorsal spine; DP, dorsal plates; B1, first basal plate; B2, second basal plate; Lateral plates, 1-10; AP, ascending process of the pelvis; VP, ventral plates; EC, ectocoracoid; P, pelvic spine; V, vertebral column; BC, body cavity: MT, musculature. (a) Location of the complex. (b) Lateral view of the complex. (c) Cross-section through the complex. Red arrows show transmission of lateral deflection of dorsal spine (large, right-pointing arrow) to lateral plates (large, left and down-pointing arrow) and to musculature (small arrows). After Reimchen (1983, 1994).

Figure 10.18 Alternative lateral plate and spine morphology in sticklebacks (*Gasterosteus aculeatus*). Reference bars are 1 cm long. (Top) Completely-plated morph, characteristic of oceanic populations. (Middle) Partially-plated morph, rare in oceanic and freshwater populations. (Bottom) Low-plated morph with reduced dorsal and pectoral spines, common in freshwater populations. From Bell (1976) with permission.

Figure 10.19 Genome-wide differentiation among stickleback populations (*Gasterosteus aculeatus*) assessed with F_{ST}. Linkage group labels are shown at the top of the figure. Colored dots indicated significantly elevated ($P \leq 10^{-5}$, blue; $P \leq 10^{-7}$, red) and reduced ($P \leq 10^{-5}$, green) values of F_{ST}. Vertical gray shading indicates boundaries of linkage groups (I – XXI) and unassembled shaffolds. Yellow shading indicates nine peaks of substantial population differentiation. (Top) F_{ST} between the two oceanic populations.

(Middle) Overall F_{ST} between the oceanic and freshwater populations. (Bottom) F_{ST} among the three freshwater populations. From Hohenlohe et al. (2010) with permission.

Figure 10.20 Details of differentiation (F_{ST}) among freshwater populations and between oceanic and freshwater populations of stickleback (*Gasterosteus aculeatus*) in Linkage Group IV. (Top) F_{ST} for each of three freshwater populations compared with the oceanic populations. Colored bars show regions of bootstrap significant ($P \leq 10^{-5}$) for each population (indicated in red, blue, and green). (Bottom) F_{ST} among the three freshwater populations (orange) and F_{ST} for the overall oceanic – freshwater comparison (black). Black bars show corresponding regions of significance ($P \leq 10^{-5}$). From Hohenlohe et al. (2010) with permission.

Figure 10.21 Divergence in the pattern of trichosomes between two *Drosophila* species reflects change in the *E* enhancers of the *svb* gene. (a) Locations of the six enhancers of *svb* (open boxes). (b) Details of the *E* enhancer in *D. melanogaster*. From Frankel et al (2011) with permission.

Figure 11.1 A correlated response to selection when the genetic correlation is negative. In these hypothetical data, truncation selection acts only on trait 1. The sample of actual parents, after selection, is shown in black, other conventions as in Fig. 10.1. Even though selection favors higher values of trait 1, trait 2 evolves in the opposite direction because of a negative genetic correlation. Recall that the regression slope is a function of the genetic covariance between the two traits.

Figure 11.2 Response to bivariate directional selection viewed as a game of pool. Directional selection, $\boldsymbol{\beta}$, is shown as a vector or cue (orange) that strikes the bivariate mean (solid blue dot), producting a response to selection, $\boldsymbol{\Delta \bar{z}}$ (thick blue vector), pointing at the bivariate mean after the response to selection (open blue dot). The G-matrix is shown as a 95% confidence elipse (blue), with major and minor axes (eigenvectors) indicated with thin blue lines. Numerical values for the elements of the G-matrix are shown in the inset matrix. (a) Response to selection on trait 1 when the G-matrix is circular. (b) Reponse to selection on trait 1 when the major axis of $\boldsymbol{G}$ is at a positive angle to $\boldsymbol{\beta}$. (c) Response to selection on trait 1 when the major axis of $\boldsymbol{G}$ is at a negative angle to $\boldsymbol{\beta}$. (d) Angles and magnitude of selection response shown as a function of seven different angles for $\boldsymbol{\beta}$.

Figure 11.3 Correlated response to selection in a set of replicate populations of finite size. In the simulation depicted here, 100 lineages of moderate size ($N_e = 500$) respond to a very weak directional selection ($\beta_1 = 0.01$) on another weakly correlated trait ($G_{12} = 0.032$). The trajectories of the correlated lineage responses (shown in black) reflect both response to selection and drift. The 99% confidence limits for the overall lineage response are shown with dotted blue lines. The deterministic correlated response to selection is shown as a white line.

Figure 11.4 Direct and correlated responses to long-term selection for increased egg production in turkeys. (a) Direct response to selection for increased egg production

(eggs/hen, expressed as deviations from a control line). Egg production is shown at three hen ages: 84 days (crosses), 180 days (solid triangles), and 260 days (open circles). (b) Unexpected correlated response of male body weight to selection for increased egg production (kg, expressed as deviations from a control line). Weights are shown at 4 male ages: 8 weeks (open circles), 18 weeks (solid triangles), 24 weeks (solid circles), and 20 weeks (crosses). After Nestor et al. (1996).

Figure 11.5 Correlated response of sternopleural bristle count to selection on abdominal bristle count in *Drosophila melanogaster*. (a) Correlated response in selected lines (n = 240 in each line). Three independent lines (solid) were selected for an increased count. Three other independent lines (dotted) were selected for a decreased count. (b) Correlated response in five control lines without selection (n = 40 in each line). After Clayton et al. (1957).

Figure 11.6 Response to selection on the bivariate relationship between a pair of wing measurements in *D. melanogaster*. (a) The two measurements (dotted lines labeled D1 and D2) whose bivariate relationship was the target of deliberate selection. (b) Response to selection in bivariate trait space. The original bivariate relationship (baseline) is shown as the middle curve. The derived relationships after 16 generations of selection are shown by the upper and lower curves. The arrows show the direction of bivariate selection. Clusters of small black dots show the samples of 100 males measured at generation 16. From Weber (1990) with permission.

Figure 11.7 Evolutionary trajectories of principal components of morphology in two species of Galápagos finches over a 30 year period. Mean values for principal component scores are shown with solid circles (*G. fortis*) and triangles (*G. scandens*). Confidence intervals for means (95%) are shown as brackets. From Grant and Grant (2002) with permission.

Figure 11.8 Viability selection differentials for principal component scores in two species of Galápagos finches over a 30 year period. The asterisks above and below the bars indicate statistical significance, ranging from * $P < 0.05$ to ****$P < 0.001$. From Grant and Grant (2002) with permission.

Figure 11.9 Geographic variation in the head and dorsal body coloration patterns of the Milk Snake (*Lampropeltis triangulum*) in the United States. The map shows the sampling of localities in the United States. Dotted lines show the boundaries between the ranges of adjacent subspecies. Areas of intergradation are indicated with stippling. Solid circles indicate locations of specimens examined by the author, open circles indicate locations of literature records or museum specimens. Insets around the map show coloration patterns on the head/neck and on the body. Body coloration consists of brown or red blotches (shown in dark gray) surrounded by a black border. The central color of the blotches is brown in *L. t. triangulum*, but red in all other subspecies. Blotches are separated light brown (shown in light gray) or white areas. The form found on the coastal plain of North Carolina, South Carolina, Georgia, and Alabama and throughout Florida is generally recognized as a separate species (*L. elapsoides*). From (Williams 1978) with permission.

Figure 11.10 Contour plot of geographic variation in body size (PC I) of female House Sparrows (*Passer domesticus*). A generalized contour plot of the geographic surface of locality mean values for PC I is shown for females (n=594 individuals from 85 localities). The largest specimens are found in areas with the darkest contours. The contour interval is $0.23\sqrt{P}$, where P is the within-population variance in PC I. From Johnston and Selander (1971) with permission.

Figure 12.1 Simpson's concept of trait evolution within and between adaptive zones. Evolution of a trait mean is indicated with lines that show branchings (speciation) and terminations (extinctions) inside and outside of adaptive zones. The lower band represents a stable zone within which lineages proliferate but trait evolution is bounded. The upper, slanting band represents a steadily changing range of environmental conditions or opportunity. Within this adaptive zone evolving trait means show a pronounced trend that occurs in parallel in related lineages. After Simpson (1944).

Figure 12.2 Simulations of replicate populations evolving about a stationary intermediate optimum. 99% confidence limits, calculated using (12.6) are shown as dotted blue curves. (a) A single lineage mean in a population of finite size evolving according to an OU process. (b) The lineage means of 25 replicate populations evolving according to the same process.

Figure 12.3 Equilibrium distributions of lineage means under weak stabilizing selection as a function of population size. Distributions of lineage means, $\Phi(\bar{z}_\infty)$, as a function of effective

population size, N_e, calculated using (12.8). (a) Weak stabilizing selection, $\Omega = 100$. (b) Very weak stabilizing selection, $\Omega = 500$.

Figure 12.4 Simulations of lineages evolving according to the early-burst model of Blomberg et al. (2003). 99% confidence limits calculated using (12.6), other conventions as in Fig. 12.3. The parameter describing diminution of drift variance is set to $r = -0.05$. (a) A simulation of one evolving lineage. (b) A simulation with 100 replicate lineages.

Figure 12.5 The Uyeda et al. (2011) data plotted with percent change in body size as a function of the length of the sampled time interval. The plot combines data from microevolutionary studies, fossils, and phylogenetic trees, revealing a pattern shaped the barrel of a blunderbuss. The two purple lines denote a $\pm$ 65% change in body size, which is approximately equivalent to $\pm 6\sqrt{P}$. The inset outlines show the change in body size in one horse lineage data point. From Arnold (2014).

Figure 12.6 Lande's adaptive landscape model with two adaptive peaks. A critical parameter in the model is the ratio of the height of the first adaptive peak at a, ($\bar{W}_a$), to the height of the valley between the peaks at v, ($\bar{W}_v$). From Estes and Arnold (2007).

Figure 13.1 Bivariate evolution on a Gaussian adaptive landscape, the spaceship model. The adaptive landscape is shown in red: the ellipse represents the equivalent 50% confidence region, with eigenvectors shown as dashed red lines. Stabilizing selection of equal magnitude acts on each trait: $\Omega_{11} = \Omega_{22} = 50$. G-matrices (represented as 95% confidence

ellipses) are shown in blue. In each case, the genetic variance of both traits is 0.4. Evolutionary trajectories of the bivariate mean are shown in black, with arrows at regular intervals of elapsed generations. (a) $r_g = r_s = 0$. Each evolutionary trajectory is 500 generations in duration, with arrowheads every 50 generations. (b) $r_g = 0.9, r_s = 0$. Each evolutionary trajectory is 1500 generations in duration, with arrowheads every 300 generations. (c) $r_g = 0, r_s = 0.9$. Each evolutionary trajectory is 500 generation in duration, with arrowheads every 50 generations. (d) $r_g = 0.9, r_s = 0.8$. Each evolutionary trajectory is 700 generations in duration, with arrowheads every 50 generations. Animations of the panels in this figure are available at https://phenotypicevolution.com/?p=102.

Figure 13.2 Values of the directional selection gradient during a simulated approach of the trait mean to a stationary adaptive peak. The values for directional selection on trait 1 (n=199) are plotted for the trajectory beginning at ($\bar{z}_1 = -10, \bar{z}_2 = 5$) in Fig 13.1c.

Figure 13.3 Stochastic response of the bivariate mean to a Gaussian adaptive landscape for 500 generations in 8 replicate lineages. No genetic correlation, $r_s = 0.9$ and $N_e = 500$. Other conventions as in Figure 13.1c, except that elapsed intervals are not indicated with arrowheads.

Figure 13.4 Distribution of estimates of genetic correlations between the sexes for homologous traits. The histogram summarizes 488 estimates from 114 sources, including both plants and animals. After Poissant et al. (2010).

Figure 13.5 The role of the adaptive landscape in shaping the results of drift-selection balance. In each panel the black line shows the results of 1000 generations of simulated evolution of the lineage mean, $\bar{\mathbf{z}}_t$, in a single lineage under the conditions specified in each panel. Each trajectory begins at the origin and ends at a point denoted by a solid red dot. Effective population size is 100. The 95% confidence ellipse for genetic values is shown in solid blue and represents the G-matrix. The adaptive landscape is bivariate stabilizing in all cases and is represented by its 25% confidence ellipse in red. Such a low level ellipse must be employed, because the limits of the 95% ellipse would be far outside the scale limits of the figure. The limiting pattern for dispersion of lineage means, $Var(\bar{\mathbf{z}}_\infty)$, is represented by its 95% confidence ellipse in dotted blue, calculated using (13.11). (a) Weak stabilizing selection with no selectional correlation and no genetic correlation. (b) Very weak stabilizing selection with no selectional correlation and no genetic correlation. Notice the change in scale. (c) Very weak stabilizing selection with strong positive selectional correlation and no genetic correlation. (d) Very weak stabilizing selection with strong positive selectional correlation and a strong negative genetic correlation. (e) Weak stabilizing selection with strong positive selectional correlation and a strong positive genetic correlation. (f) Weak stabilizing selection with strong positive selectional correlation and a strong negative genetic correlation. Animations of these figures are available at https://phenotypicevolution.com/?page_id=33.

Figure 13.6 Absolute values of the directional selection gradient during a simulation of drift-selection balance. The values for directional selection on trait 1 (n=1000) are for the trajectory beginning at $\bar{z}_1 = 0, \bar{z}_2 = 0$ in Fig 13.5c and lasting for 1,000 generations.

Figure 13.7 Predators and mates exert opposing forces of selection on a male ornament. In this hypothetical example, selection by the peahen on the peacock's tail favors a larger, more complex tail, while selection by a predator (the tiger) favors small tails that promote more rapid escape. Drawing by Dafila Scott. From Stearns and Hoekstra (2000) with permission.

Figure 13.8 Lande's (1981) model for the deterministic evolution of a male ornament and female mating preference based on that ornament. The stable case is illustrated. The solid red line is the line of equilibria. The dashed red line shows the position of the viability selection optimum, θ, for the male ornament. Solid black lines show evolutionary trajectories for 12 starting positions, with arrows, denoting the response to selection, spaced every generation. The blue ellipses at the starting points are 95% confidence ellipses for the G-matrices. Parameter values are: $G = H = 0.4; B = 0.24;\ \omega = 4, \alpha = 0.1, P = 1, \theta = 0$. The similarity between $\boldsymbol{g}_{max}$ and the line of equilibria in this figure is a coincidence.

Figure 13.9 Simulations of Iwasa and Pomiankowski's (1995) model for perpetual evolution of a male ornament and a female mating preference. The evolutionary trajectories of two sets of 10 replicate lineages are shown with origination at $\bar{z} = \bar{y} = 0$, with simulation

durations of 1,000 (above) and 2,000 generations (below). Red dots show the positions of each bivariate lineage mean at the end of the simulation. In this model the line of equilibria, the red curves in the panels on the left, is a cubic function. This line of equilibria consists of stable and unstable zones. The transition to flanking stable zones is shown as grey bands. The central unstable zone is located between the grey bands. Populations off the line of equilibria evolve deterministically along trajectories with a slope of B/G; one such line (thin black) is shown through the origin. (a and b) On a 1,000 generation timescale, the tendency of lineages to stall within the zones of stability (at or beyond the grey bands) is apparent. (c and d) The 2,000 generation timescale in this simulation provides more opportunities for transit between the two stable zones. Indeed, two lineages have evolved across the unstable zone, from one stable zone to the other, and another lineage has entered the unstable, central zone. Parameter values are: $N_e = 10^6, G = H = 0.5, B = 0.05, a = 0.4, b = 0.001, c = 0.05, u = 0$ (unbiased mutation).

Figure 13.10 Sexual selection exaggerates the evolution of male ornaments and female preferences, producing a phenotypic tango. The evolution of the two male ornament means (blue dots) and the two female preference means (red dots) are superimposed in 2-dimensional trait space. Trait means for a particular lineage are connected by thin black line. Means of 100 lineages are shown after 500 generations of evolution in response to natural and sexual selection. The 95% confidence limits for this sample of male ornament and female preference means are shown respectively as light blue and light red ellipses. The expected 95% confidence limits for male ornament and female preference means evolving in response to natural selection alone are shown as heavy ellipses (optima are

shown as dots at the center of these ellipses). Crucial parameters are: $N_e = 5000;\ P_{ii} = Q_{ii} = 1;\ G_{ii} = H_{ii} = 0.4;\ B_{ii} = 0.24;\ \boldsymbol{\omega_z} = (4, 0, 0, 4)^{\mathrm{T}}, \boldsymbol{\omega_y} = (19, 0, 0, 19)^{\mathrm{T}}$. $\boldsymbol{Q}$ is the female analog of the male phenotypic matrix $\boldsymbol{P}$. For other parameters and details see Arnold and Houck 2016, Fig. 4B.

Figure 13.11 Simulated ornament and preference means evolving for 100,000 generations showing that the PTM can match observed divergence in birds-of-paradise ornament traits. Ornament (blue) and preference (red) means are shown in units of within-population standard deviation ($\sqrt{P_{ii}}$ and $\sqrt{Q_{ii}}$). Black curves show the expected 99% confidence limits for ornament evolution in response to natural selection alone. Bold red lines show the comparable limits for preference evolution. Dotted red lines show two times the 99% confidence limits for preferences. Simulation of 25 lineages with $N_e = 500;\ P_{ii} = Q_{ii} = 1;\ G_{ii} = H_{ii} = 0.4;\ B_{ii} = 0.24;\ \boldsymbol{\omega_z} = (9, 0, 0, 9)^{\mathrm{T}}, \boldsymbol{\omega_y} = (9999, 0, 0, 9999)^{\mathrm{T}}$. See Arnold and Houck (2016) for more details and parameter values.

Figure 13.12 Simulated evolution of ornament and preference traits with a moving preference optimum. Conventions and parameter values as in Fig. 13.11, except $N_e = 5000;\ \boldsymbol{\omega_y} = (19, 0, 0, 19)^{\mathrm{T}}$ (these values correct errors in Fig. 7 caption in Arnold and Houck 2016) and $\sigma_\theta^2 = 0.00055$. The orange curve shows expected 95% confidence limits for diversification of preference means evolving in response to a moving natural selection optimum, using expression (13.29). From Arnold and Houck (2016).

Figure 13.13 Two male birds-of-paradise (*Paradisaea apoda*) displaying to a female, showing the role of the wings and tail in forming a static shape. The evolution of the lengths of the male wings and tails across the *Paradisaea* radiation are analyzed in Table 13.1. From Arnold and Houck (2016).

Figure 14.1 Simulations of lineages evolving in response to white noise motion of the optima of the AL. In these simulations the long term average position of the optimum and the lineage means is zero, indicated with thin white lines. (a) The trait mean of a single lineage (above) evolving in response the movement of the optimum of its AL, shown in the next panel. The red dot shows the position of the trait mean at the end of the simulation. The blue dotted lines show the upper and lower 99% confidence limits of the average trait mean, calculated using (14.1). (b) The position of the optimum as a function of time. The orange dot shows the position of the optimum at the end of the simulation. The red dotted lines show the upper and lower 99% confidence limits of the optimum. (c) The trait means of 10 replicate lineages evolving in response the movement of their optima, shown in the next panel. The red dots show the position of the trait means at the end of the simulation. (d) The positions of ten replicate optima as a function of time. The orange dots show the position of the optima at the end of the simulation.

Figure 14.2 Simulations of the response of lineage trait means to an intermediate optimum that undergoes Brownian motion. Graphic conventions as in Fig. 14.1. (a) The trait mean of a single lineage mean closely tracks the moving optimum of its AL, shown in next panel. (b) The movement of the trait optimum. (c) The trait means of 100 replicate lineage means

closely track the moving optima of their ALs, shown in next panel. (d) The movement of 100 trait optima.

Figure 14.3 Simulations of lineages evolving in response to a steadily moving intermediate optiumum with superimposed white noise fluctuations in position. Conventions as in Fig. 14.1. The position of the optimum increases in value at a rate of 0.005 within-population standard deviation per generation ($k = 0.005$). (a) The trait mean of a single lineage evolving in response to a moving optimum, shown in next panel. (b) Movement of the optimum of the AL. (c) The trait means of 10 replicate lineages evolving in response to the movement of their optima, shown in next panel. (d) Movement of the optima of 10 replicate moving optima.

Figure 14.4 A simulation of a trait mean evolving in response to its steadily moving optimum in which the rate of motion of the optimum is 25 times slower than in Fig. 14.3. The parameter for peak movement is $k = 0.0002$. The means of more lineages exceed the the 99% confidence limit (dotted blue and red lines) than in Fig. 14.3 because the simulation lasts 50,000 rather than 400 generations. (a) Simulated evolution of the trait means of 10 replicate lineages. The 99% confidence limits of the mean (thin white line) is barely visible. The violet line shows divergence equivalent to $6\sqrt{P}$. (b) The simulated trait optima of 100 replicate lineages. Same conventions as in Fig. 14.3.

Figure 14.5 Gaussian version of a double OU process. The trait distribution (blue) has a mean $\bar{z}(t) = 0$ at time t and a variance of $P = 1$. The Gaussian adaptive landscape (red)

has an optimum $\theta(t) = 1$ at time t and a width of $\Omega = 10$. The Gaussian peak controller function (purple) has an optimum $\Psi = -1$ and a width of $\Upsilon = 30$.

Figure 14.6 Simulation of a single trait mean of a single population evolving in response to a single displacement of its adaptive peak. (a) The evolving trait mean (thin black line) and its 99% confidence limits (dotted blue curve), calculated using (14.23). (b) The displacement of the adaptive peak by $5\sqrt{P}$ occurs instantaneously in generation 1. Conventions as in Fig. 14.3.

Figure 14.7 Time course for the loss of three anti-predator structures in a fossil lineage of stickleback. (a) Number of dorsal spines. (b) Number of touching pterygiophores. (c) Pelvic score. From Hunt et al. (2008) with permission.

Figure 14.8 Simulations of 8 lineages evolving in response to different displacements of their intermediate optima. At generation 0, the position of the optima ranges from -6 to 6 and at generation 1 those optima are displaced by 3.5 to $9\sqrt{P}$. Red dots show the positions of lineage means at the end of the simulation.

Figure 14.9 Simulation of the single-burst model against a background of white noise movement of the adaptive peak. The red line shows the position of the optimum. Parameter values are $\sigma_\theta^2 = 5$, $\sigma_d^2 = 37$, and $\lambda = 0.005$. The average waiting time for a displacement of the optimum is $1/\lambda = 200$ generations. The 99% confidence limits for a normal distribution with mean zero and variance $\sigma_\theta^2 = 5$ are shown in violet. In this run, a

single displacement of the optimum occurs at about generation 150. Conventions as in Fig. 14.8.

Figure 14.10 Distributions of lineage means after various elapsed times according to the single-burst model. Parameter values are $\sigma_\theta^2 = 5$, $\sigma_d^2 = 87.5$, and $\lambda = 0.0001$. The average waiting time for a displacement of the optimum is $1/\lambda = 10{,}000$ generations. The 99% confidence limits for a normal distribution with mean zero and variance $\sigma_\theta^2 = 5$ are shown in violet.

Figure 14.11 Simulation of 10 replicate lineage trait means evolving according to the single-burst model. The red lines show the position of the optima, which undergo a single displacement in each lineage. Parameter values are $\sigma_\theta^2 = 0.1$, are $\sigma_d^2 = 10$, and $\lambda = 0.01$. The average waiting time for a displacement of the optimum is $1/\lambda = 100$ generations. Typical bounds for actual data are shown in violet.

Figure 14.12 Simulation of the multiple-burst model for evolution of the trait mean in a single lineage. The red line shows the position of the optimum evolving by multiple bursts. Parameter values are $\sigma_\theta^2 = 5$, $\sigma_d^2 = 37$, and $\lambda = 0.005$. The average waiting time for a displacement of the optimum is $1/\lambda = 200$ generations. The 99% confidence limits for a normal distribution with mean zero and variance $\sigma_\theta^2 = 5$ are shown in violet. In this example, three displacements occur, at about 220, 550, and 675 generations.

Figure 14.13 Distributions of lineage means after five different elapsed times according to the multiple-burst model. Parameter values are $\sigma_\theta^2 = 5$, $\sigma_d^2 = 37$, and $\lambda = 0.00001$. The average waiting time for a displacement of the optimum is $1/\lambda = 100{,}000$ generations. The 99% confidence limits for a normal distribution with mean zero and variance $\sigma_\theta^2 = 5$ are shown in violet.

Figure 14.14 Maximum likelihood estimates of parameters for the best-fitting multiple-burst model. (a) Plot of the Uyeda et al. 2011 data. (b) Gaussian curves representing the white noise distribution (mean = 0, standard deviation = 0.096) and the burst size distribution (mean = 0 , standard deviation = 0.272). (c) Burst timing distribution, showing the waiting times between bursts ($1/\lambda$) obtained by bootstrapping over studies (2,000 replicates). The vertical red dashed lines show the position of the average waiting time on the actual and simulated data plots. From Arnold (2014).

Figure 14.15 Graphical comparison of the best-fit versions of the Brownian motion, single-burst, and multiple-burst models. Silhouettes of the data points are shown in grey (same data as shown in Fig. 14.14a, except that pairwise tree data are not included). The blue lines show the 99% confidence limits corresponding to the parameters fit by maximum likelihood. Divergence is measured as the difference between the means of log-transformed size, standardized by dimensionality. (a) Fit of the Multiple-burst model. (b) Fit of the Single-burst model. (c) Fit of the Brownian motion model. From Arnold (2014).

Figure 15.1 Simulated evolution of genetic variance (upper panels) and genetic kurtosis (lower panels) under mutation-drift-selection balance over 5,000 generations. (Left side)

The straight lines show the average values for genetic variance (0.285) and genetic kurtosis (3.12) for a single run with $N_e = 683$, $(\omega + 1) = 10$, $\mu = 0.0002$, and a normal distribution of mutant alleles with $\alpha^2 = 0.05$. (Right side) The average values for genetic variance and genetic kurtosis are 0.233 and 6.27, respectively, for a single run with $N_e = 171$, $(\omega + 1) = 10$, $\mu = 0.0002$, and a reflected gamma distribution of mutant alleles with $\alpha^2 = 0.05$. From Bürger and Lande (1994) with permission.

Figure 16.1 The average G-matrices of inbred lines are smaller and proportional to the G-matrices of outbred control lines. Each diagram shows the G-matrices (95% confidence ellipses) for a pair of traits (see labels for principal axes above each diagram). Each outer ellipse represents the G-matrix for outbred controls, while each inner ellipse the average G-matrix for inbred lines. From Phillips et al. (2001) with permission.

Figure 16.2 Variation in G-matrices for a single pair of traits (B vs. F) among inbred lines (n = 52). The ellipse for the outbred control is shown at the center of the panel. Conventions as in Fig. 16.1. From Phillips et al. (2001) with permission.

Figure 16.3 In simulations, the G-matrix tends to evolve towards alignment with the M-matrix and the adaptive landscape. Each row shows the results of a single 2,000 generation simulation run. The first three ellipses in each row show the 95% confidence ellipses for mutation ($\boldsymbol{M}$), the adaptive landscape ($\boldsymbol{\Omega} = \boldsymbol{\omega} + \boldsymbol{P}$), and the average G-matrix (shown on different scales). The last 8 ellipses in each row show the G-matrix every 200 generations during the run. From top to bottom the values of r_μ and r_ω are: (a) $r_\mu = r_\omega = 0$; (b)

$r_\mu = 0,\ r_\omega = 0.75$; (c) $r_\mu = 0.5,\ r_\omega = 0$; (d) $r_\mu = 0.5, r_\omega = 0.75$; (e) $r_\mu = r_\omega = 0.90$. From Arnold et al. (2008) with permission.

Figure 16.4 Simulations illustrating the effects of the orientation of the *M*-matrix and the adaptive landscape on the size and eccentricity of the *G*-matrix. (Left panel) Time series for the size of the *G*-matrix (sum of eigenvalues) when (a) $r_\mu = r_\omega = 0$; (b) $r_\mu = 0,\ r_\omega = 0.75$; (c) $r_\mu = 0.5,\ r_\omega = 0$; (d) $r_\mu = 0.5, r_\omega = 0.75$; (e) $r_\mu = r_\omega = 0.90$. (Right panel) Time series for the eccentricity of the G-matrix (smaller eigenvalue divided by larger eigenvalue) with parameters (a) through (e) as in Left panel. From Jones et al. (2003) with permission.

Figure 16.5 The *M*-matrix tends to evolve toward alignment with the adaptive landscape. In the simulations summarized here, the mutational correlation (r_μ) was allowed to evolve while orientation of the adaptive landscape was varied. In different runs the selectional correlation (r_ω) was held constant at 0.90 by varying the elements of the ω-matrix, so that the orientation of the leading eigenvector of the adaptive landscape (angle of correlational selection varied from about 19−45 degrees. Each green point is the mean of 50 replicate runs ($\pm$ s.e.). Data from Jones et al. (2007), plot after Arnold et al. (2008).

Figure 16.6 Triple alignment of selection, genetic variation, and mutation is promoted by epistasis. In each of three sets of simulation runs, the ω -matrix was held at three different values (orange matrices in the first vertical panel, orange ellipse in the second vertical panel). G-matrices (blue matrices, blue ellipses) and M-matrices (green matrices, green

ellipses) were allowed to evolve in response to those specified selection surfaces. As the angle of the selection surface ($\boldsymbol{\omega_{max}}$) is rotated, the angles of $\boldsymbol{G}$ and $\boldsymbol{M}$ evolve in response resulting in triple alignment of the three matrices. From Jones et al. (2014) with permission.

Figure 16.7 The evolution of the G-matrix in response to selection and migration. (a) The selection and migration scheme. Selection surfaces are shown as red ellipses. The G-matrix is shown as a blue ellipse. The trait optimum (intersection of the dotted red lines) for the mainland population is located at the center of the circle (shown in black). The G-matrix has evolved to equilibrium with the configuration and position of the selection surface. The trait optimum for an island population is at one of five positions on the circle. The solid straight lines connect the optimum of the mainland with the optimum of each island population. This line is the *expected line of divergence* (LoD) for the bivariate island mean. The black arrows show the directional selection that acts on the island trait mean as it begins its evolutionary trajectory. (b) The evolution of the G-matrix in response to the selection-migration scheme shown on the left. The mainland and island G-matrices are shown as black ellipses. The position of the trait optimum is shown by a red cross inside a red circle. Correlational selection denoted r_s is the same as r_ω. The evolutionary trajectory of the bivariate trait mean for one simulation run for each island configuration is represented by black dots, shown at intervals of 10 generations. From Guillaume and Whitlock (2007) with permission.

Figure 16.8 Effects of strong migration on the orientation and shape of the *G*–matrix for two traits. Correlational selection denoted r_s is the same as r_ω. (a) No correlational selection, strong mutational correlation. (b) Strong correlational selection, no mutational correlation. (c) Strong correlational selection and strong mutational correlation. (d) Strong negative correlational selection, strong positive mutational correlation. From Guillaume and Whitlock (2007) with permission.

Figure 16.9 Numbers of tail and body vertebrae in samples of newborn females from two California populations of the garter snake *T. elegans*. Females from the inland population are shown as light blue dots (n = 690), females from the coastal population are shown as dark blue dots (n = 474). Least squares regression lines the regression of tail count on body count are shown for both populations. Data are from the study reported by (Arnold and Phillips (1999) and Phillips and Arnold (1999).

Figure 16.10 The Flury hierarchy for comparing *G*-matrices is a nested series of hypotheses thare are tested by comparing eigenvalues and eigenvectors. The illustrated hierarchy is for the comparison of bivariate *G*-matrices, represented by their 95% confidence ellipses. CPC refers to common principal components, the sharing of eigenvectors, even though eigenvalues may differ. From Arnold et al. (2008).

Figure 16.11 Comparison of *G*-matrix ellipses of males and females of the coastal and inland populations of *Thamnophis elegans* showing the common principal component result. The

figure shows projections of the first two principal components onto the tail (subcaudal) and body (ventral scale count) axes. From Arnold and Phillips (1999).

Figure 16.12 Graphical summary of empirical comparisons of *G*-matrices. Only the 31 studies that made comparisons using the Flury hierarchy are included here. From left to right, the four panels summarize results from 4 kinds of studies: conspecific populations exposed to different environmental treatments (n = 63 pairwise comparisons), males versus females from the same population (n = 12), conspecific populations sampled from nature (n = 97), and different species sampled from nature (n = 32). Outcomes of statistical tests are classified into the categories described in Fig. 16.10. Full CPC means that matrices had all principal components (eigenvectors) in common; partial CPC means that at least one but not all principal components were in common. Some studies compared multiple pairs of matrices, and in such cases, all the outcomes are tabulated. From Arnold et al. (2008).

Figure 16.13 Phylogenetic comparison of morphometric *P*-matrix ellipses from eight species of *Anolis* lizards. The phylogeny is shown in the first column. Columns 2—6 show 95% confidence ellipses for pairs of morphometric traits. The five illustrated pairs of trait measurements are: humerus vs. femur (hu-f), lamellae 4th vs. femur (l-f), pelvis vs. humerus (p-f), head width vs. lamellae 4th (hw-l), and head width vs. femur (hw-f). After Kolbe et al. (2011).

Figure 17.1 Evolution and stability of the G-matrix when the optimum is steadily moving. In these simulations, the optimum is steadily moving to the right ($\Delta\theta_1 = 0.007\sqrt{P}$), so that the optimum value for trait 1 is constantly changing, but the optimum value for trait 2 is constant. The G-matrix is represented by its 95% confidence ellipse, shown at 300 generation intervals. The position of the optimum in the same generation as the G-matrix snapshot is shown with the small, filled circle. Parameter values are: $N_e = 342$, $\omega_{11} = \omega_{22} = 49$. From Jones et al. (2004).

Figure 17.2 Contrasting conditions for G-matrix stability. The configuration of the AL is shown in red contours. The location of the adaptive peak (red-filled small circles) is moving up and to the right. Snapshots of the G-matrix, represented by 95% confidence ellipses (blue), are shown at 300 generation intervals. The configuration of the M-matrix is shown with green ellipses. (a) The absence of correlational selection and correlated mutation results causes instability in the orientation of the G-matrix. (b) Three-way alignment of mutation, the AL and peak movement produces a very stable G-matrix. Parameter values are: $N_e = 342$, $\omega_{11} = \omega_{22} = 49$, $N_e = 342$, $r_\mu = 0$ or 0.9, $r_\omega = 0$ or 0.9. Simulation data from Jones et al. (2004).

Figure 17.3 Schematic portrayals of the three modes of peak movement used in the Jones et al. (2012) simulations. In all of these figures, the peak starts at the origin and moves up and to the right. (a) The peak moves every generation for 1000 generations in a constant direction at a constant rate ($\Delta\theta_1 = \Delta\theta_1 = 0.0071$). (b) The peak jumps to a new position every 100 generations ($\Delta\theta_1 = \Delta\theta_1 = 0.071$). (c) The peak moves every generation

($\Delta\theta_1 = \Delta\theta_1 = 0.0071$), but peak movement also includes an element of Brownian motion stochasticity each generation (see section 14.2 for the model). In the illustrated simulation, the stochasticity variance parameter (σ_θ^2) was 0.01. The orange dot shows the final position of the optimum at generation 1000. After Jones et al. (2012).

Figure 17.4 Times series from a single simulation run showing responses of some aspects of the G-matrix to a steadily moving optimum, in which the optimum is moving in a positive direction for both traits (↗). In this example, $\omega_{11} = \omega_{22} = 9$, $r_\omega = 0$, $r_\mu = 0.5$, $\Delta\theta_1 = \Delta\theta_2 = 0.007\sqrt{P}$, $N_e = 1024$. From Jones et al. (2012).

Figure 17.5 Time series from a single simulation run showing responses of some aspects of the G-matrix to an optimum that moves episodically every 250 generations in the same direction and at the same long-term average rate as in Figure 17.4. All other parameter values are identical to those used for Figure 17.4. From Jones et al. (2012).

Figure 17.6 The effect of rate of peak movement on trait modularity. Faster rates of peak movement establish more pronounced modularity. Each bar shows the 95% confidence limits for the mean of 10 simulations after 10,000 generations. The mean is indicated by a black dot. Faster rates of movement result in smaller between-module correlation and hence larger sampling variance in the AVG ratio. The peak moved at rates varying from 0.0001 to 0.004, which are expressed in units of within-lineage environmental variation. Parameter values in the simulations were: $N_e = 5{,}000$, per locus mutation rate = 5×10^{-4},

per locus mutational variance = 0.02, $\omega_{ii} = 10$ and $\omega_{ij} = 8$ within-modules, $\omega_{ii} = \omega_{ij} = 0$ between modules, 500 loci, 10 traits). From Melo and Marroig (2015) with permission.

Figure 17.7 The establishment of modularity by correlational selection. At generation zero (after a 20,000 generation burn-in period), correlational selection was established in the lineages shown in green, but not in the lineages shown in red. Gray bars show the 95% confidence limit for the mean of 50 replicates. Means are shown in colors. Parameter values as in Fig. 17.6. From Melo and Marroig (2015) with permission.

Figure 17.8 Maintenance of modularity by correlational selection and loss of modularity under regimes of drift and uncorrelated selection. During the 20,000 generation burn-in period, modularity was established in all lineages by directional selection. Beginning at generation 30,000 directional selection ceased. In addition all stabilizing and correlational selection ceased in the 100 drift lineages (shown in green), only stabilizing selection was maintained in the 100 uncorrelated stabilizing selection lineages (blue), whereas correlated and stabilizing selection was maintained in the 1000 correlated selection lineages (red). All other parameter values as in Fig. 17.6 and graphic conventions as in Fig. 17.7. From Melo and Marroig (2015) with permission.

Figure 18.1 An interpretation of bivariate evolution of vertebral numbers in natricine snakes. The data for this example are plotted in Fig. 9.2 and 9.3. Here we superimpose identical hypothetical adaptive landscapes for each population (red dotted contour plots), assuming that the landscapes are homogeneous in shape and size and that population

means are located close to their optima. The long axes of the selection surfaces represent a common $\boldsymbol{\omega_{max}}$. The principal axis of dispersion ($\boldsymbol{d_{max}}$) is shown as the long double-headed black arrow, which coincides with the major axis of SSLR movement of the adaptive peaks. The minor axis of dispersion ($\boldsymbol{d_{min}}$) is shown as the short double-headed black arrow, which coincides with the minor axis of SSLR movement of the adaptive peaks.

Figure 18.2 Simulations of evolution along selective lines of least resistance. Simulated evolution of 25 replicate bivariate trait means in response to Brownian motion of their bivariate optima along the leading eigenvector of their adaptive landscapes for 1,000 generations. Effective population size is 500. Cases of modest (r = 0.5), strong (r = 0.9), and very strong correlation (r = 0.98) in inheritance, selection, and peak movement are illustrated. Evolutionary trajectories of trait means and optima are shown with black lines. The positions of replicate trait means and optima after 1,000 generations are shown with red and orange circles, respectively. Expected outcomes after 1,000 generations are shown with 95% confidence ellipses based on expression (18.4) for optima (orange, dotted ellipses) and lineage trait means (blue, dotted ellipses). The leading and trailing eigenvectors of these ellipses are shown with dotted lines. In these simulations, the leading eigenvectors of the G– matrix, Ω- matrix, and Br- matrix are identical. (a) Evolution of 25 replicate trait means with $\boldsymbol{G}$ = (0.4 0.2, 0.2 0.4), and $\boldsymbol{\Omega}$ = (10 5, 5 10). (b) Brownian motion of 25 replicate bivariate optima with $\boldsymbol{Br}$ = (0.001 0.0005, 0.0005 0.001). (c) Evolution of 25 replicate trait means with $\boldsymbol{G}$ = (0.4 0.36, 0.36 0.4), and $\boldsymbol{\Omega}$ = (10 9, 9 10). (d) Brownian motion of 25 replicate bivariate optima with $\boldsymbol{Br}$ = (0.001 0.0009, 0.0009 0.001). (e) Evolution of 25 replicate trait means with $\boldsymbol{G}$ = (0.4 0.392, 0.392 0.4),

and $\boldsymbol{\Omega} =$ (10 9.8, 9.8 10). (f) Browinan motion of 25 replicate bivariate optima with $\boldsymbol{Br} =$ (0.001 0.00098, 0.00098 0.001).

Figure 18.3 Conceptual diagram illustrating selection for bilateral symmetry and the evolution of bilateral traits in the direction of SLLR movement. (a) Selection on bilateral traits can be visualized in two related frames of reference. In the first frame of reference (solid box), the trait axes are the scores on the left and right sides of the organism. Selection favoring bilateral symmetry is a cigar-shaped ISS (orange ellipse) in which the major axis is equality of left and right side scores, shown as a dashed orange line from the lower left to the upper right corner. The minor axis of the selection surface is a dashed orange line from the upper left to the lower right corner. Stabilizing selection is much stronger along this axis than along the major axis. We expect that this correlational selection surface will promote correlation between left and right sides and produce a trait distribution before selection (shown as a blue ellipse) that is aligned with the selection surface. In the second frame of reference (dotted box), the axes are rotated 90 deg. One of the new axes is the sum or average of left and right sides. Stabilizing selection is relatively weak along this axis. The orthogonal axis is the differences between left and right sides. Stabilizing selection is strong on this axis and favors zero difference between left and right sides. (b) The expected directions of evolution of trait averages in replicate populations is shown as a double-headed black arrows, which represent the major and minor directions of SLLR movement. Each evolving trait mean (blue dot) tracks the peak of its adaptive landscape, shown as a dashed, red ellipse. These peaks tend to move along the major axis of the adaptive landscape, which is equivalent to equality of left and right side averages,

and to a much lesser extent along the minor axis of the adaptive landscape, which is equivalent to difference between left and right side averages.

Figure 18.4 Metabolic rate as a function of temperature and mass in various organisms. (a) Mass-corrected metabolic rate, $\ln\left(IM^{-3/4}\right)$ as a function of temperature, $1/kT$, measured in degrees Kelvin (K). (b) Temperature-corrected metabolic rate, $\ln(I\ e^{E/kT})$, measured in watts, as a function of body mass, $\ln(M)$, measured in grams. From Brown et al. (2004) with permission.

Figure 18.5 Survival of juvenile song sparrows as a function of wing length and body mass. (a) Fitness contours reveal a ridge with a slope of about 0.75 mm/g. Circles indicate the bivariate phenotypes of individuals that survived (filled) or disappeared (open). (b) A three dimensional representation of the selection surface. From Schluter and Nychka (1994) with permission.

Figure 18.6 Horn length as a function of body size (prothorax width) in a base population of dung beetles (*Onthophagus acuminatus*). (a) The original sigmoidal bivariate relationship. (b) The almost unimodal distribution of body size. (c) The strongly bimodal distribution of horn size. After Emlen (1996).

Figure 18.7 Dung beetle horn length as a function of body size after 7 generations of bidirectional selection. Selection for increased (blue circles denote up line) and decreased

(green circles denote down line) residual horn length caused a lateral divergence in the sigmoidal relationship. After Emlen (1996).

Figure 19.1 Two examples of sexual isolation between pairs of populations whose mean values for ornaments and preferences have diverged along the line of evolutionary equilibrium. The upper panels show the positions of male and female trait means on the line of equilibrium. Population A is shown in purple and population B is shown in green The lower panels show the distributions of male ornaments ($p(z)$, solid curves) and female preferences ($\psi(z)$, dotted curves). (a) Modest trait divergence between the two populations resulting in a modest level of sexual isolation ($JI = 0.89$). (b) Profound trait divergence resulting in a nearly maximal value for sexual isolation ($JI = 1.95$). Parameter values for this these examples are $P = Q = 1$, and $\nu = 5$; see column 19.2a in Table 19.1. From Uyeda et al. (2009).

Figure 19.2 Two pairs of simulated evolutionary trajectories for sexual isolation. The dotted line corresponds to $JI = 1.6$ which represents a substantial level of isolation (see text). In each pair of populations (purple and green) joint isolation (JI) waxes and wanes as trait means of each population drift away from and towards each other. Parameter values in both examples are $G = H = 0.6$, $\omega = 50$, $\nu = 5$, and $N_e = 1000$. From Uyeda et al. (2009).

Figure 19.3 Distributions of sexual isolation (JI) over 10,000 generations of simulated evolution. Results from 10,000 independent pairs of populations are shown, including

mean isolation (solid curve) and standard deviation (dashed curves). Histograms of the distribution of JI are shown at 2,000 generation intervals, with shaded bars indicating substantial sexual isolation ($JI > 1.6$). Parameter values as in Fig. 19.2. From Uyeda et al. (2009).

Figure 19.4 Joint evolution of two ornament traits and two mating preference traits undergoing the Fisher-Lande process in a finite population with natural selection on ornaments but not on preferences. Ornament means are shown in open circles and preference means are shown in solid. Ornament and preference means in the same generation are connected by solid black lines, but are often not visible because the means of the two sexes are close together. Means are plotted every 200 generations and preference means are connected by gray lines. One population is shown in green, the other in purple. The simulation begins with the means of both populations at the origin and ends with the means far apart in the upper left and upper right corners of the plot. The trajectories result from 10,000 generations of interactions between drift ($N_e = 1000$) and selection. The genetic variance of male and female traits is 0.6. Traits are genetically uncorrelated within sexes. Genetic correlations between the sexes are 0.6 for traits with the same subscript and 0 otherwise. For both ornaments, $\omega = 50$ (with no correlational selection), and $P = 1$; for both preferences, $\nu = 0.4$ (with no correlational preferences), $Q = 1$, and $\alpha = 0.1$. The simulation begins with all traits at the values of the optimum of the ornaments traits (x-axis value = 0, y-axis value = 0), at the center of the figure.

Figure 19.5 Time course for joint isolation, *JI*. The hortizontal dashed line shows the lower level of *JI* that is characteristic of sympatric, isolated species. *JI* values computed from the simulation shown in Fig. 19.4.

Figure 19.6 Joint evolution of two ornament traits and two preference traits in replicate pairs of populations undergoing the Fisher-Lande process in a finite populations with natural selection on ornaments but not on preferences. Results are shown after 10,000 generations of simulation using parameters listed in Fig. 19.4. (a) Haystack Plot showing divergence between ornament means in 100 replicate pairs of populations. Each line connects the ornament means of a replicate pair of populations. (b) Histogram of Joint Isolation measures for the 100 pairs of populations. The dashed line shows the expected level of reproductive isolation ($JI = 1.6$) expected in sympatric pairs; 77% of pairs have achieved that level of isolation or higher. This distribution has a mean of 1.61 and a variance of 0.30.

Figure 19.7 Latent trait axes for male and female traits that mediate sexual isolation in *Desmognathus* salamanders, inferred from a survey of sexual isolation. Male trait means (blue) and female trait means (red) from the same population are connected by solid lines. Dotted lines enclose populations currently assigned to three different species (Tilley and Mahoney 1996). From Hohenlohe and Arnold (2010).

Figure 19.8 The transition from the pursuit to persuasion phase of courtship in the salamander *Plethodon metcalfi*. (a) After pursuing the female (stippled), the male (unstippled) touches her cheek with his snout. (b) The male crawls under her chin, lifting

his head as he does so. (c) The male's body contacts her chin as he slides forward. (d) The male stops, while arching and undulating his tail under her chin. If the female steps astride the female's tail, the persuasion phase of courtship begins. From Arnold (1976) with permission.

Figure 19.9 Joint evolution of two ornaments and two preferences in two populations undergoing the Fisher-Lande process with drift and stabilizing selection on ornaments and preferences. Same graphic conventions as in Fig. 19.4, with same parameter values (column 19.d in Table 19.1). The width parameter for Gaussian stabilizing selection on each of four traits is $\omega = 50$.

Figure 19.10 Evolutionary time course for joint isolation, *JI*, in two populations undergoing the Fisher-Lande process with drift and stabilizing selection on ornaments and preferences. The horizontal dashed line shows the lower level of JI that is characteristic of sympatric, isolated species. JI values computed from the simulation shown in Fig. 19.9.

Figure 19.11 Joint evolution of two ornaments and two preferences in 100 replicate pairs of populations undergoing the Fisher-Lande process with drift and stabilizing selection on ornaments and preferences. Results are shown after 10,000 generations of simulation using the parameters listed in Fig. 19.9. (a) Haystack plot showing divergence between ornament means in 100 replicate pairs of populations. Each line connects the ornament means of a replicate pair of populations. (b) Histogram of Joint Isolation measures for the

100 pairs of populations. This distribution has a mean of 0.012, a variance of 0.00014, and a range of -0.0014 to 0.061.

Figure 19.12 The evolution of two ornament and two preference traits in response to Brownian motion of both the natural selection optima of ornaments and preferences and with sexual selection on the ornaments. Movement of optima generation-by-generation is shown over 10,000 generations of the simulation: ornament optima are shown in yellow, preference optima shown in orange. Trait means are shown in two separate plots, rather than superimposed as in Fig. 19.4. Graphical conventions as in Fig. 19.4, but because of the larger scale, ornament and preference means in the same generation (connected by black line) appear to be closer together. Parameters as in Fig. 19.4, except for Brownian motion of optima with per-generation variance of $\sigma_\theta^2 = 0.00055$ for both traits in each sex in each population. The simulation begins with the values for the bivariate optima of ornaments and preferences at the center of the figure (x-axis value = 0, y-axis value = 0). (a) Evolution in population A in response to Brownian motion of its optima. Trait and preference means (open and solid purple circles) are shown every 200 generations. (b) Evolution in population B in response to independent Brownian motion of its optima. Trait and preference means (open and solid green circles) are shown every 200 generations.

Figure 19.13 The evolution of two ornament and two preference traits in response to Brownian motion of their natural selection optima for preferences (but not ornaments) and with sexual selection on the ornaments. Graphic and simulation parameters as in Fig. 19.12.

Brownian motion of natural selection optima for preferences with per-generation variance of $\sigma_\theta^2 = 0.00055$ for both preference traits in each population. (a) Evolution in population A in response to Brownian motion of its preference optima. (b) Evolution in population B in response to Brownian motion of its preference optima.

Figure 19.14 The evolution of two ornament and two preference traits in response to Brownian motion of their natural selection optima for ornaments (but not preferences) and with sexual selection on the ornaments. Graphic and simulation parameters as in Fig. 19.12. Brownian motion of natural selection optima for ornaments with per-generation variance of $\sigma_\theta^2 = 0.00055$ for both ornament traits in each population. (a) Evolution in population A in response to Brownian motion of its ornament optima. (b) Evolution in population B in response to Brownian motion of its ornament optima.

Figure 19.15 Evolutionary time courses for joint isolation, *JI*, between two populations undergoing the Fisher-Lande process with drift and stabilizing selection on ornaments and/or preferences. Optima of ornaments and/or preferences move by Brownian motion each generation. JI values computed from the simulation shown in Fig. 19.12-14. The hortizontal dashed line shows the lower level JI that is characteristic of sympatric, isolated species. (a) Evolution of JI when both ornament and preference optima undergo Brownian motion. JI values computed from the simulation shown in Fig. 19.12. (b) Evolution of JI when only the preference optima undergo Brownian motion. JI values computed from the simulation shown in Fig. 19.13. (c) Evolution of JI when only the ornament optima undergo Brownian motion. JI values computed from the simulation shown in Fig. 19.14.

Figure 19.16 Joint evolution of two ornament traits and two mating preference traits undergoing the Fisher-Lande process with natural selection optima moving by Brownian motion. Results are shown after 10,000 generations of simulation using parameters listed in Fig. 19.12. (**First row**) Both ornament and preference optima undergo Brownian motion: (a) haystack plot showing divergence between ornament means in 100 replicate pairs of populations. Each line connects the ornament means of a replicate pair of populations, (b) histogram of Joint Isolation measures for the 100 pairs of populations (two pairs with slightly negative JI are omitted from the plot) . The dashed line shows the expected level of reproductive isolation ($JI = 1.6$) expected in sympatric pairs of species; 5% of pairs have this level of isolation or higher. This distribution has a mean of 0.75, a variance of 0.25 and a range of -0.0049 to 1.925. (**Second row**) Only preference optima undergoes Brownian motion: (c) haystack plot showing divergence between ornament means in 100 replicate pairs of populations, (d) Histogram of Joint Isolation measures for the 100 pairs of populations. The dashed line shows the expected level of reproductive isolation ($JI = 1.6$) expected in sympatric pairs of species; 1% of pairs have this level of isolation or higher. This distribution has a mean of 0.49, a variance of 0.16, and a range of 0.0002 to 1.71. (**Third row**) Only ornament optima undergoes Brownian motion: (e) haystack plot showing divergence between ornament means in 100 replicate pairs of populations, (f) histogram of Joint Isolation measures for the 100 pairs of populations. The dashed line shows the expected level of reproductive isolation ($JI = 1.6$) expected in sympatric pairs of species; 2% of pairs achieved this level of isolation. This distribution has a mean of 0.42, a variance of 0.15, and a range of 0.0026 to 1.82.

Figure 19.17 The evolution of two habitats traits in each sex in response to Brownian motion of their natural selection optima. Parameters as in Fig. 19.12 except each trait experiences only natural selection towards an intermediate optimum as well as drift (compare columns 19.2e and 19.3a in Table 19.1). Graphic conventions as in Figure 19.12. (a) Male and female habitat traits in population *A* evolving in response to the same Brownian motion of a natural selection optimum (shown in orange). (b) Male and female habitat traits in population *B* evolving in response to the same Brownian motion of a natural selection optimum. This Brownian motion is independent of the BM experienced by population *A.*

Figure 19.18 Evolutionary time courses for ecological isolation, *EI*, between two populations responding to Brownian motion of male and female optima for habitat traits. Optima of the traits move independently by Brownian motion each generation in each population. The horizontal dashed line shows the lower level of *EI* that is characteristic of joint isolation in sympatric, isolated species. *EI* values computed from the simulation shown in Fig. 19.17.

Figure 19.19 Joint evolution of two habitat traits each in males and females in 100 replicate pairs of populations with Brownian motion of natural selection optima. Results are shown after 10,000 generations of simulation using the parameters listed in Fig. 19.12. (a) Haystack plot showing divergence between habitat trait means in 100 replicate pairs of populations. Each line connects the habitat trait means of a replicate pair of populations. (b) Histogram of Ecological Isolation measures for the 100 pairs of populations. The vertical dashed line shows the expected level of reproductive isolation ($EI = 1.6$) expected

in sympatric pairs of species; 38% of pairs have this level of isolation or higher. This distribution has a mean of 1.24, a variance of 0.34, and a range of 0.03 to 1.99.

Figure 19.20 The evolution of two ecological niche traits in response to Brownian motion of their natural selection optima. Parameters as in Fig. 19.12 except each trait experiences only natural selection towards an intermediate optimum and drift (compare columns 19.2e and 19.3b in Table 19.1). Graphic conventions as in Fig. 19.12. (a) Two niche traits in population *A* evolving in response to the same Brownian motion of a natural selection optimum (shown in orange). (b) Two niche traits in population *B* evolving in response to bivariate Brownian motion of a natural selection optimum. This Brownian motion is independent of the BM experienced by population *A.*

Figure 19.21 Evolutionary time course for ecological distance, *ED*, between two populations responding to Brownian motion of the optima for two ecological traits. Optima of the traits move independently by Brownian motion each generation in each population. *ED* values computed from the simulation shown in Fig. 19.20.

Figure 19.22 Joint evolution of two ecological niche traits in 100 replicate pairs of populations whose natural selection optima move by Brownian motion. Results are shown after 10,000 generations of simulation using the parameters as in Fig. 19.20. (a) Haystack plot showing divergence between trait means in 100 replicate pairs of populations. Each line connects the trait means of a replicate pair of populations. (b) Histogram of Ecological

Distance for the 100 pairs of populations. This distribution has a mean of 4.02, a variance of 4.68, and a range of 0.84 to 11.56.

Figure 19.23 The evolution of two traits that mediate competition between two species in response to Brownian motion of their natural selection optima. Parameters as in Fig. 19.9, except each trait experiences only natural selection towards an intermediate optimum and drift (compare columns 19.2e and 19.3c). Graphic conventions as in Figure 19.12. (a) Two competition-mediating traits in population *A* evolving in response to Brownian motion of a bivariate natural selection optimum (shown in orange). (b) Two competition-mediating traits in population *B* evolving in response to Brownian motion of a bivariate natural selection optimum. This Brownian motion is independent of the BM experienced by population *A*.

Figure 19.24 Evolutionary time course for ecological distance, *ED*, between two populations responding to Brownian motion of the optima for two competition-mediating traits. Optima of the traits move independently by Brownian motion each generation in each population. (a) *ED* values computed from the simulation shown in Fig. 19.23. (b) *ED* values computed from a replicate simulation showing a strikingly different outcome. Simulation parameters as in Fig. 19.23.

Figure 19.25 Evolution of ecological distance, *ED*, between two populations responding to Brownian motion of the optima for two competition-mediating traits. Results are shown after 10,000 generations of simulation using the same parameters as in Fig. 19.24. (a)

Haystack plot showing divergence between trait means in 100 replicate pairs of populations. Each line connects the trait means of a replicate pair of populations. (b) Histogram of Ecological Distance for the 100 pairs of populations. This distribution has a mean of 4.32, a variance of 5.18, and a range of 0.65 to 9.98.

Figure 20.1 Coevolution of a floral trait and a matching pollinator trait according to the model of Kiester et al. 1984. The line of stable equilibria is shown in red. Coevolutionary trajectories, lines of motion (black), are shown from 14 starting points with arrowheads every 10 generations. Parameter values are $G_x = G_y = 0.4, P = P_x = P_y = 1, \tau_x = \tau_y = 1, \eta = 1, v^2 = 4$.

Figure 20.2 Interaction success as a function of difference in insect and plant trait means. Three examples are shown for $\alpha = 0.005$, 0.2, and 1.5. After Nuismer 2017.

Figure 20.3 Functional success as a Gaussian function of trait values. In this example, the optimum is $\theta_x = 0$ and the width variable is $\omega_x = 49$.

Figure 20.4 Path diagram and network depiction of the model for two interacting species. The plant species is shown in green and the insect species is shown in blue. (Left) Path diagram showing how the selection gradients ($\beta_{xI}, \beta_{xF}, \beta_{yI}, \beta_{yF}$) translate the effects of an intermediate optimum (θ_x, θ_y) and the species interaction between the trait means of the two species ($\bar{x}, \bar{y}$) to effects on the population mean fitness of the two species ($\bar{W}_X, \bar{W}_Y$). The curved arrows are meant to show that interaction selection gradients in each species

(β_{xI}, β_{yI}) are functions of the trait means of both species. (Right) Network diagram, a symbolic version of the path diagram.

Figure 20.5 Coevolution of an plant trait and an interacting insect trait according to a model by Nuismer 2017. The location of the joint intermediate optima for the two traits is shown as a solid orange dot at the intersection of dotted orange lines. The coevolutionary equilibrium $(\hat{x}, \hat{y})$ is shown as a solid blue dot. Coevolutionary trajectories (black lines) are shown from 8 starting positions. (a) Straight coevolutionary trajectories arise from symmetrical variables for the two species ($G_x = G_y = 0.4, s_X = s_Y = 0.1, \alpha = 1.5,$ $\theta_x = \theta_y = 0, \omega_x = \omega_y = 49$). Arrowheads are shown every 50 generations for 450 generations. The blue dot at the evolutionary equilibrium is hidden by arrowheads. (b) Curved coevolutionary trajectories are due to asymmetrical stabilizing selection ($\omega_x = 49, \omega_y = 99$) with all other parameters as in the preceeding case. Arrowheads positioned every 50 generations for 600 generations.

Figure 20.6 Network diagram of a parasite X with two traits (blue boxes) interacting with the traits of two host species Y and Z (green boxes). Population mean fitnesses are shown as circles. The genetic correlation between the two parasite traits is shown as a double−headed dotted arrow. Other conventions as in Fig. 20.4.

Figure 20.7 Interaction success as a matching, quadratic function of the difference in trait values, (20.35). In this example, $\alpha = 0.05$.

Figure 20.8 Coevolution of a host trait and one of two interacting parasite traits. Graphic conventions as in Fig. 20.5. Arrowheads every 50 generations for 500 generations. Parameter values used in calculations: $G_{x,11} = G_{x,22} = 0.4, G_y = G_z = 0.4$, $s_y = s_z = s_{x,1} = s_{x,2} = 0.01, \theta_y = \theta_z = \theta_{x,1} = \theta_{x,2} = 0$, $\omega_y = \omega_z = \omega_{x,1} = \omega_{x,1} = 49$. Companion plots of the mean of host trait, $\bar{z}$, as a function of the mean of the parasite trait, $\bar{x}_2$, were identical to the plots shown here. (a) Coevolutionary trajectories of the mean of host trait, $\bar{y}$, as a function of the mean of the parasite trait, $\bar{x}_1$, when the genetic correlation between the two parasite traits is zero ($G_{x,12} = 0$). (b) Coevolutionary trajectories of the mean of host trait, $\bar{y}$, as a function of the mean of the parasite trait, $\bar{x}_1$, when the genetic correlation between the two parasite traits is 0.9 ($G_{x,12} = 0.36$). (c) Coevolutionary trajectories of the mean of parasite trait 2 , $\bar{x}_2$, as a function of the mean of the parasite trait 1, $\bar{x}_1$, when the genetic correlation between the two parasite traits is zero ($G_{x,12} = 0$). (d) Coevolutionary trajectories of the mean of parasite trait 2 , $\bar{x}_2$, as a function of the mean of the parasite trait 1, $\bar{x}_1$, when the genetic correlation between the two parasite traits is 0.8 ($G_{x,12} = 0.32$).

Figure 20.9 Coevolution of a prey trait and one of two interacting predator traits. Graphic conventions as in Fig. 20.5. The genetic correlation between the two predator traits is zero ($G_{x,12} = 0$) in the first row of three graphs, 0.8 ($G_{x,12} = 0.32$) in the second row, and , 0.8 ($G_{x,12} = -0.32$) in the third row. Arrowheads every 50 generations for 500 generations in the top row. Arrowheads every 50 generations for 1000 generations in the middle and bottom rows. Parameter values used in all calculations: $G_{x,11} = G_{x,22} = 0.4, G_y = G_z = 0.4$, $s_y = s_z = 0.01, s_{x,1} = s_{x,2} = 0.05, \theta_y = \theta_z = \theta_{x,1} = \theta_{x,2} = 0$, $\omega_y = \omega_z = \omega_{x,1} = \omega_{x,1} = 49$. Companion plots of the mean of prey trait, $\bar{z}$, as a function of the mean of the predator trait,

$\bar{x}_2$, were identical to the plots shown here. (a) Coevolutionary trajectories of the mean of prey trait, $\bar{y}$, as a function of the mean of the predator trait, $\bar{x}_1$, when the genetic correlation between the two predator traits is zero. (b) Coevolutionary trajectories of the mean of predator trait 2 , $\bar{x}_2$, as a function of the mean of predator trait 1, $\bar{x}_1$, when the genetic correlation between the two parasite traits is zero ($G_{x,12} = 0$). (c) Coevolutionary trajectories of the mean of prey trait, $\bar{y}$, as a function of the mean of the predator trait, $\bar{x}_1$, when the genetic correlation between the two predator traits is 0.8. (d) Coevolutionary trajectories of the mean of predator trait 2 , $\bar{x}_2$, as a function of the mean of predator trait 1, $\bar{x}_1$, when the genetic correlation between the two parasite traits is 0.8 ($G_{x,12} = 0.32$). (e) Coevolutionary trajectories of the mean of prey trait, $\bar{y}$, as a function of the mean of the predator trait, $\bar{x}_1$, when the genetic correlation between the two parasite traits is -0.8. (f) Coevolutionary trajectories of the mean of predator trait 2 , $\bar{x}_2$, as a function of the mean of predator trait 1, $\bar{x}_1$, when the genetic correlation between the two parasite traits is -0.8 ($G_{x,12} = -0.32$).

Figure 20.10 Network diagram of the bill traits of two bird species (blue) interacting with the fruit traits of two plant species (green). Population mean fitnesses are shown as circles; trait means are shown as boxes. Other conventions as in Fig. 20.4.

Figure 20.11 Phylogeny of three competing species. Speciation events occur at times τ_1 and τ_2. The present time is denoted τ_p. After Nuismer (2017).

Figure 20.12 Stochastic coevolution of the means of the interacting traits of a pair of competing species in drift-selection balance. Same parameter values as in Fig. 20.4a. Stochasticity is a consequence of genetic drift of the mean. Effective population size is 100 in each species. Five independent trajectories are shown, all beginning at the expected equilibrium ($\hat{x} = 1.93, \hat{y} = 1.93$), shown as a solid blue dot (almost totally obscured by the red dots), surrounded by the 95% confidence ellipse (blue circle) for coevolutionary outcome under drift-selection balance at time infinity (section 13.4). The final position of each trajectory after 500 generations is shown as a solid red dot. The position of the functional optimum is shown as a solid orange dot.

Figure 21.1 A hypothetical adaptive landscape for a single trait and the limited perspectives of this surface commonly taken by evolutionary biologists and ecologists. (a) The evolutionist's view: an adaptive landscape for a single trait under stabilizing selection. The natural logarithm of average population fitness as a function of average trait value. (b) The ecologist's view: growth rate of the population as a function of abundance evaluated at the average trait value. (c) The combined perspective. From McPeek (2017a) with permission.

Figure 21.2 Intrinsic birthrate of the resource, $c(z_R)$, is a convex quadratic function of resource trait value (z_R). In this example $c_0 = 1.0$, $\gamma_c = 0.004$, and $\theta_c = 10$.

Figure 21.3 The contribution of consumer deathrate to fitness, $-f(z_N)$, is a convex quadratic function of consumer trait value (z_N). In this example $f_0 = 0.1$, $\gamma_f = 0.01$, and $\theta_f = 4$.

Figure 21.4 Attack success, given by $a(z_R, z_N)$, is a matching Gaussian function of the difference in trait values, $(z_R - z_N)$. In this example $a_0 = 0.1$ and $\omega_a = 12.5$.

Figure 21.5 Path diagram and network depictions of McPeek's fitness model for two interacting species. The resource species is shown in green and the consumer species is shown in blue. (Left) Path diagram showing how the selection gradients (β_{zNb}, β_{zNd}, β_{zRb}, β_{zRd}) translate the effects of an intermediate optimum (θ_f, θ_c) and the species interaction between the trait means of the two species ($\bar{z}_N, \bar{z}_R$) into effects on the population mean fitness of the two species ($ln\bar{W}_N, ln\bar{W}_R$). The curved arrows remind us that the interactions selection gradients in each species (β_{zNb}, β_{zRd}) are functions of the trait means of both species. (Right) Network diagram, a symbolic version of the path diagram.

Figure 21.6 A simulated example of the dynamics of abundances and trait means during coevolution of a resource and consumer species. This figure shows different views of a single simulation lasting for 3500 iterations with the following fixed values for parameters: $c_0 = 1.0$, $d = 0.02$, $a_0 = 0.1$, $b = 0.1$, $h = 0.1$, $f_0 = 0.1$, $g = 0.0$, $\omega_a = 12.5$, $\gamma_c = 0.002$, $\gamma_f = 0.01$, $\theta_c = 10$, $\theta_f = 4$, $G_{z_R} = G_{z_N} = 0.2$ and the following initial values of variables: $\bar{z}_R = 10$, $R = 50.0$, $\bar{z}_N = 4.0$, $N = 0.01$. (a) Time course of resource abundance, R (shown in green) and consumer abundance, N (shown in blue). (b) Time course of resource and consumer trait means, $\bar{z}_R$ (shown in green) and $\bar{z}_N$ (shown in blue). The position of the two functional optima are shown with orange dotted lines. (c) Time courses of attack rate, $a(\bar{z}_R, \bar{z}_N)$ (shown in black, scale on left), intrinsic resource birthrate, $c(\bar{z}_R)$ (shown in green, scale on right), and intrinsic consumer deathrate, $f(\bar{z}_N)$ (shown in blue, scale on left). (d) Consumer trait mean ($\bar{z}_N$) as a function of resource trait mean ($\bar{z}_R$) during coevolution.

Arrowheads are shown every 200 iterations. Orange dotted lines show optimum values for consumer deathrate (θ_c, hortizontal line) and resource birthrate (θ_f, vertical line). The dotted black line show the optimum combinations of trait means specified by attack success, $a(\bar{z}_R, \bar{z}_N)$, i.e., $\bar{z}_R = \bar{z}_N$. (e) Consumer abundance (N) as a function of resource abundance (R) during coevolution. Arrowheads are shown every 75 iterations. After McPeek (2017a, b).

Figure 21.7 Trait means on evolving adaptive landscapes and their components. The resource trait mean, $\bar{z}_R$, is shown in the left column and the consumer trait mean, $\bar{z}_N$, is shown in the right column. Trait means are shown as red circles, with a solid red circle indicating the equilibrium position (final position at iteration 3400). Adaptive landscapes and their components are shown every 200 iterations as grey curves and as red curves at iteration 3400. (a) The evolving adaptive landscape of the resource species. (b) The birth component of the adaptive landscape of the resource species shifts upward and equilibrates in the configuration shown by the red curve. (c) The evolving death component of the adaptive landscape of the resource species. (d) The evolving adaptive landscape of the consumer species. (e) The evolving birth component of the consumer species. (f) The death component of the consumer's adaptive landscape does not evolve and is shown as a single red curve. See also McPeek's interactive simulator of these curves at http://enallagma.com/evolutionarycommunityecology/traitsConsumerResource.html.

Figure 21.8 Network diagram for McPeek's (2017a) model of apparent competition between two resource species (shown in green) showing that they interact with the

consumer species (shown in blue) but not with each other. Graphic conventions as in Fig. 21.5.

Figure 21.9 Eco-evolutionary dynamics drive a peak shift by a resource species (R_1). The abundance (a) and trait values (b) of two resource species with identical parameter values (R_1 in light green, R_2 in dark green) and a consumer (N_1 in blue) are shown over 4000 iterations of a simulation with the following parameter values ($c_0 = 1.0$, $d = 0.02$, $a_0 = 3.5$, $b = 0.1$, $h = 0.1$, $f_0 = 0.2$, $g = 0.0$, $\omega_a = 12.5$, $\gamma_c = 0.005$, $\gamma_f = 0.005$, $\theta_c = 12$, $\theta_f = 5$, $G_{z_R} = G_{z_N} = 0.2$) and the following initial values of variables: $\bar{z}_R = ca.\,20$, $R = ca.\,10.0$, $\bar{z}_N = ca.\,17.5$, $N = ca.\,2$. From McPeek (2017a) with permission.

Figure 21.10 Eco-evolutionary dynamics drive a peak shift by a resource species (R_1), continued. Graphic conventions as in Fig. 21.7. The adaptive landscapes of the three species (two resource species, $R_1$and R_2, and a consumer, N_1, are shown at iteration 0 (a) and iteration 4000 (b). Vertical dashed lines show the positions of mean trait values. From McPeek (2017a) with permission.

Figure 22.1 Temporal organization of courtship modules in *Rhyacotriton* and plethodontid salamanders. Courtship sequences flow from left to right (large arrows) and from top to bottom within modules. Behaviors shown in the same color occur in the same temporal context. Behaviors shown with different shades of the same color occur in a predictable; those in lighter shades occur earlier than those in darker shades. Module labels: AP = approach, HC = head contact, TSW = tail-straddling walk, SD = spermatophore deposition, and POS = positioning over spermatophore. From Arnold et al. (2017) with permission.

Figure 22.2 The final two modules in the courtship of the salamander *Ensatina*. (a) spermatophore deposition (SD-*deposit*), lateral view. (b) Spermatophore deposition (SD-*deposit*), top view. (c) Start of lift-off (POS- *lift-off*). (d) Flex (POS-*flex*) (e) Start of backup (POS-*backup*). The female is picking up the spermatophore cap. (f) *Rock* and *massage* (POS-*rock*, *massage*). From Stebbins (1949) with permission.

Figure 22.3 Temporal organization of courtship modules in four species of birds of paradise in the genus *Parotia*. Display modules are shown as labeled, gray octagonal boxes (HPP = horizontal perch pivot, HPS = horizontal perch slide, HAC = hops-across-court, CCD = court clearing dance, HT = head tilting, SB = swaying bounce, HS = hop and shake, and BD = ballerina dance). Courtship sequences flow from left to right (large arrows) and from top to bottom within modules. Colored rectangles denote phases within modules. Phases are of six major kinds (inset box). Alternative versions of phase sequences are shown as side-by-side columns within modules. From Scholes (2008) with permission.